SciPost Physics

Submission

Efficient and Flexible Approach to Simulate Low-Dimensional Quantum Lattice Models with Large Local Hilbert Spaces

T. Köhler[1], J. Stolpp[2], S. Paeckel[3*]

1 Department of Physics and Astronomy, Uppsala University, Box 516, S-751 20 Uppsala, Sweden **2** Institut für Theoretische Physik, Georg-August-Universität Göttingen, 37077 Göttingen, Germany **3** Department of Physics, Arnold Sommerfeld Center for Theoretical Physics (ASC), Munich Center for Quantum Science and Technology (MCQST), Ludwig-Maximilians-Universität München, 80333 München, Germany
* sebastian.paeckel@physik.uni-muenchen.de

Abstract

Quantum lattice models with large local Hilbert spaces emerge across various fields in quantum many-body physics. Problems such as the interplay between fermions and phonons, the BCS-BEC crossover of interacting bosons, or decoherence in quantum simulators have been extensively studied both theoretically and experimentally. In recent years, tensor network methods have become one of the most successful tools to treat such lattice systems numerically. Nevertheless, systems with large local Hilbert spaces remain challenging. Here, we introduce a mapping that allows to construct artificial $U(1)$ symmetries for any type of lattice model. Exploiting the generated symmetries, numerical expenses that are related to the local degrees of freedom decrease significantly. This allows for an efficient treatment of systems with large local dimensions. Further exploring this mapping, we reveal an intimate connection between the Schmidt values of the corresponding matrix-product-state representation and the single-site reduced density matrix. Our findings motivate an intuitive physical picture of the truncations occurring in typical algorithms and we give bounds on the numerical complexity in comparison to standard methods that do not exploit such artificial symmetries. We demonstrate this new mapping, provide an implementation recipe for an existing code, and perform example calculations for the Holstein model at half filling. We studied systems with a very large number of lattice sites up to $L = 501$ while accounting for $N_{\mathrm{ph}} = 63$ phonons per site with high precision in the CDW phase.

1 Introduction

Large local Hilbert spaces appear in various kinds of problems in quantum many-body physics. Prominent examples arise in the field of ultra-cold quantum gases. Systems such as interacting bosons in a one-dimensional lattice [1, 2] or trapped ion quantum simulators [3–5] have been studied extensively, fertilizing a rapid theoretical and experimental progress. Another typical problem featuring large local Hilbert spaces is the interplay between lattice fermions and phonons. For instance, the formation and stability of (Bi-)Polarons is a central problem and considerable effort has been taken for its investigation [6–15]. A broad class of different methods such as quantum Monte Carlo [16, 17], density-functional theory [18], density-matrix embedding theory [19], or dynamical mean-field theory [20–22] has been explored to study its various aspects. Evidently, the task to numerically describe such low-dimensional, strongly correlated quantum systems has been subject to a vast development. In particular, the capabilities of tensor-network methods have improved a lot in the past two decades. Here, matrix-product states (MPSs) have become the fundament for flexible, numerically unbiased and in principle exact methods allowing for the study of not only ground-state properties but also of out-of-equilibrium dynamics of quantum many-body systems [23–33].

In (time-dependent) density-matrix renormalization group (DMRG) methods, the computationally limiting factor is the bond dimension of the tensors when performing tensor contractions [26–28, 30, 31, 33]. For instance, using MPS, one is mostly concerned with matrix-matrix contractions, which scale with the third power of the dimensions of the involved matrices. However, these operations can be rendered cheaper if the system under consideration conserves global symmetries. Being able to exploit (non-)abelean symmetries is an important feature of tensor networks in general [34–37], as a large bond dimension is related to the amount of entanglement and decay of correlation functions [29, 38, 39]. Aiming to describe strongly correlated systems, large bond dimensions can be required and thereby exploiting as many symmetries of the system as possible is highly desired.

Another important contribution to the numerical expenses of MPS algorithms is the dimension of the local Hilbert spaces $\mathcal{H}_j$. For instance, when considering systems with large spin or bosonic degrees of freedom, a local dimension $\dim \mathcal{H}_j \equiv d_j \sim \mathcal{O}(10) - \mathcal{O}(100)$ can yield drastic restrictions on the maximum possible bond dimensions as typical contractions usually scale with d_j^2 or even d_j^3. In order to overcome such restrictions, approaches such as the pseudo site (PS) and the local-basis optimization (LBO) method [6, 40–42] were developed. These methods have proven to be successful tools for treating fermion-phonon couplings in the Holstein model, even out of equilibrium and at finite temperature [6, 10, 13, 14].

In this paper, we introduce an alternative approach to simulate systems with large local Hilbert spaces efficiently and in a flexible framework. In order to treat these kinds of systems efficiently with MPS, we exploit the fact that global $U(1)$ symmetries reduce effective local block dimensions drastically [34–36]. The starting point of our method is a thermofield doubling of the many-body Hilbert space, which is an established procedure in finite-temperature DMRG [43–45]. Then, introducing a new representation for operators in a particular subspace of the doubled Hilbert space allows us to show that global operators breaking $U(1)$ symmetries can be identified with *projected purified operators* that conserve the corresponding symmetries[1]. Thereby, challenging general lattice systems breaking global $U(1)$ symmetries with $d_j \sim \mathcal{O}(10) - \mathcal{O}(100)$ can always be mapped into numerically more feasible systems. Importantly, this mapping requires only minor changes in existing codes and is completely general.

The paper is organized as follows: At first, we present the relevant aspects of our approach in Sec. 2 in a non-technical fashion and provide an implementation recipe that captures the changes in actual codes. In Sec. 3, we introduce the *projected purification* in great detail and show how to construct corresponding operators. In Secs. 4 and 5, we present the representation in terms of MPS. This includes the observation in Sec. 5.1 that connects the singular values of auxiliary bond indices with the diagonal elements of the single-site reduced density matrix, yielding an intuitive physical criterion to decide when the projected purification provides numerical benefits. We also discuss the numerical complexity of this mapping in actual calculations in Sec. 5.2. We close our discussion in Sec. 6 with an exemplary application of our mapping to physical Hamiltonians, i.e., the Holstein model and a Hubbard model with pair creation and annihilation and present some numerical results for the former.

2 General Concept and Implementation Recipe

The general idea of our mapping is to exploit global $U(1)$-symmetries, where the system under consideration does not conserve them in the first place. In the tensor-network framework, states can be constructed so that they transform under a global symmetry, i.e., they are eigenstates of the corresponding symmetry generator. Let us consider a system with a global particle number operator $\hat{N}$. Eigenstates $|N\rangle$ of $\hat{N}$ are labeled by their irreducible representations N and (ignoring degeneracies) any state can be decomposed in terms of these eigenstates

$$|\psi\rangle = \sum_N \psi_N |N\rangle \ . \tag{1}$$

Now, we can perform a doubling of the original Hilbert space and construct states of the form

$$|\psi\rangle_{PB} = \sum_{N,N'} \psi_{N,N'} |N\rangle_P \otimes |N'\rangle_B \ , \tag{2}$$

where we introduced labels P, B to distinguish the different Hilbert spaces. We restrict the allowed coefficients N' such that each state $|N\rangle$ can be mapped uniquely to a state $|N\rangle_P \otimes |N_0 - N\rangle_B$ with a properly chosen N_0:

$$|N\rangle \longmapsto |N\rangle_P \otimes |N_0 - N\rangle_B \ . \tag{3}$$

---

[1]A side note: The construction is closely related to the formulation of supersymmetry in high-energy physics. Even though, supersymmetry itself is not possible for lattice systems by construction, the general prescriptions of our method show striking similarities [46].
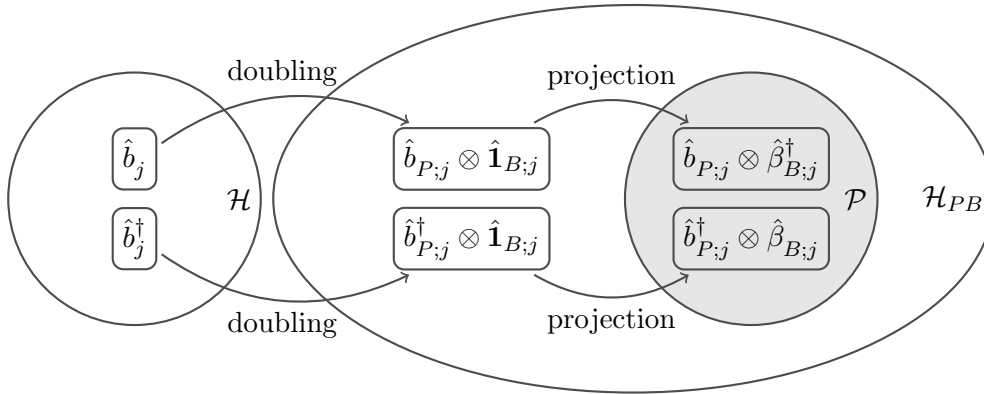
Figure 1: Mapping of local operators $\hat{b}_j$ and $\hat{b}_j^\dagger$ acting on $\mathcal{H}$ into projected purified local operators $\hat{b}_{P;j}\hat{\beta}_{B;j}^\dagger$ and $\hat{b}_{P;j}^\dagger\hat{\beta}_{B;j}$ acting on $\mathcal{P}$. This transformation is the central, necessary modification for existing codes in order to use our method.

The transformed wavefunctions

$$|\psi\rangle \longmapsto \sum_N \psi_{N,N_0} |N\rangle_P \otimes |N-N_0\rangle_B \tag{4}$$

are eigenstates of the new, global symmetry $\hat{N}_P + \hat{N}_B$ with eigenvalue N_0 and can therefore be represented efficiently by symmetric MPS. The subspace $\mathcal{P}$ spanned by all states $|N\rangle_P \otimes |N_0 - N\rangle_B$ has the same dimension as the original Hilbert space so that no additional complexity is generated with this new representation. Importantly, the same considerations can be applied to the local degrees of freedom, constituting the many-body Hilbert space.

Guided by this idea we will show in the following sections that there is a simple prescription to transform operators so that they are acting in $\mathcal{P}$ only. Using balancing operators $\hat{\beta}_{B;j}^{(\dagger)}$ (which are introduced in Eqs. (17) and (18)), global operators $\hat{O}$ that break the global $U(1)$ symmetry generated by $\hat{N}$ can be mapped into operators conserving the global $U(1)$ symmetry generated by $\hat{N}_P + \hat{N}_B$. This is achieved by replacing ladder operators $\hat{b}_j^{(\dagger)}$ in the original Hilbert space:

$$\begin{aligned}\hat{b}_j &\longmapsto \hat{b}_{P;j} \otimes \hat{\beta}_{B;j}^\dagger \\ \hat{b}_j^\dagger &\longmapsto \hat{b}_{P;j}^\dagger \otimes \hat{\beta}_{B;j} \, .\end{aligned} \tag{5}$$

The detailed mapping, containing also the intermediate step of doubling the Hilbert space, is shown in Fig. 1.

Recapitulating this short description of the general ideas of our mapping it should be noted that the states mapped to $\mathcal{P}$ are pure states in $\mathcal{P}$ but describe mixed states with respect to the orthogonal decomposition of $\mathcal{H}$ in terms of the eigenstates of $\hat{N}$. This is in close reminiscence to the purification procedure [43–45] that is commonly used to represent mixed states with respect to $\mathcal{H}$. However, there is also an important difference: Restricting the allowed states by a projection into the subspace $\mathcal{P}$ of the doubled Hilbert space, the complexity of the state's representation is conserved, i.e., our mapping does not add additional degrees of freedom to the problem under consideration.

Next, we provide a short recipe, for how to implement the previously described projected purified DMRG (ppDMRG) for ground-state searches and time-evolution methods, including prerequirements. Note that this recipe is particularly short, because the necessary changes are small.

Prerequirements In order to incorporate ppDMRG into an existing framework, it is necessary that the framework can handle Hamiltonians with more than nearest-neighbor interactions.

Necessary changes The existing set of local operators needs to be extended with balancing operators that act on the bath sites, as introduced in Eqs. (17) and (18). In particular, for every species of local creation and annihilation operators corresponding balancing operators are needed when changing a global $U(1)$ quantum number. Those operators shall only have zero and one as elements and always commute with every other operator. Additionally, for each species of creation- and annihilation operators $\hat{b}_j^{(\dagger)}$, a parity-operator $\hat{P}_{\hat{b}_j} = e^{\mathrm{i}\pi \hat{b}_j^\dagger \hat{b}_j}$ might be useful. A scenario in which the action of $\hat{P}_{\hat{b}_j}$ is necessary is discussed in Sec. 6.

Usage Following these changes, all existing tools can be used as usual, but with a doubled system size where physical and bath sites alternate, which is a common technique in finite-temperature DMRG. Hence, local observables are now evaluated via two neighboring operators. However, care must be taken that the MPS represents states in $\mathcal{P}$, i.e., the L local gauge constraints defined in Eq. (16) have to be fulfilled. Fortunately, since projected purified operators manifestly act on $\mathcal{P}$ only, it suffices to ensure that the initial state of any algorithm is in $\mathcal{P}$. For instance, using the previous conventions, an initial state for a ground-state search is given by the product state

$$|\psi) = |n_{P;1} = 0\rangle \otimes |n_{B;1} = \sigma - 1\rangle \otimes \cdots |n_{P;L} = 0\rangle \otimes |n_{B;L} = \sigma - 1\rangle \ . \tag{6}$$

Clearly, for typical ground-state calculations this state is a bad initial guess. However, it can be used as a starting point to create more suitable initial guess states by applying sequences of projected purified operators.

3 General Models and Bath Sites

We consider a lattice system of $L \in \mathbb{N}$ degrees of freedom, each of which being described within a Hilbert space $\mathcal{H}_\sigma$ of local dimension $\sigma \in \mathbb{N}$ spanning the system's overall tensor-product Hilbert space $\mathcal{H} = \mathcal{H}_\sigma^{\otimes L}$. A state $|\psi\rangle \in \mathcal{H}$ can be expressed in terms of all local degrees of freedom $|\sigma_1 \cdots \sigma_L\rangle \in \mathcal{H}$:

$$|\psi\rangle = \sum_{\sigma_1, \ldots, \sigma_L} \psi_{\sigma_1 \ldots \sigma_L} |\sigma_1, \ldots, \sigma_L\rangle \ , \tag{7}$$

with, in general, complex coefficients $\psi_{\sigma_1 \ldots \sigma_L} \in \mathbb{C}$.

Let $\hat{O}$ be an operator acting on this tensor product Hilbert space $\mathcal{H}$ and let $\hat{N} = \sum_j \hat{n}_j$ be another operator with local operators $\hat{n}_j : \mathcal{H}_\sigma \longmapsto \mathcal{H}_\sigma$ fulfilling the commutation relations $[\hat{n}_j, \hat{n}_k] = 0$. We denote the ladder operators spanning the algebra of local operators by $\hat{b}_j^{(\dagger)}$ that obey canonical commutation relations $\left[\hat{b}_j, \hat{b}_k^\dagger\right]_\epsilon = \delta_{j,k}$ and $\epsilon = \pm$ distinguishes between the commutator or anticommutator. Without loss of generality, we choose the spectrum of the local operators $\hat{n}_j$ to be $n_j \in \{0, 1, \ldots, \sigma - 1\}^2$. Let us assume furthermore that $\hat{O}$ contains summands with ladder operators $\hat{b}_j^{(\dagger)}$ that are not

---

²In fact, the following discussion is valid for any labeling of the irreducible representations of the $U(1)$ symmetries.
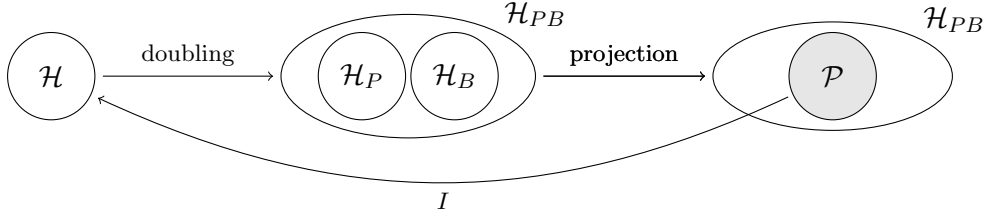
Figure 2: Starting from some Hilbert space $\mathcal{H}$, a thermofield doubling is performed to obtain the combined Hilbert space $\mathcal{H}_{PB} = \mathcal{H}_P \otimes \mathcal{H}_B$. Applying the projection as discussed in the main text yields the subspace $\mathcal{P}$, in which the global $U(1)$ symmetry is restored. Finally, upon acting with I as introduced in Eq. (12), states in $\mathcal{P}$ are identified with states in $\mathcal{H}$.

paired up with their Hermitian conjugates breaking the global $U(1)$ symmetry generated by $\hat{N}$. For instance, in the Holstein model (see Sec. 6.1) such contributions are given by the fermion-phonon interactions

$$\hat{O} = -\sum_j \hat{n}_j^f \left(\hat{b}_j^\dagger + \hat{b}_j \right) \quad \Rightarrow \left[\hat{N}, \hat{O} \right] \neq 0 \,. \tag{8}$$

Note that in this example $\hat{N} = \sum_j \hat{b}_j^\dagger \hat{b}_j$ is the operator counting the number of phonons and $\hat{n}_j^f$ measures the local fermion density.

Next, we introduce a thermofield doubling of this Hilbert space. The new double Hilbert space $\mathcal{H}_{PB} = \mathcal{H}_P \otimes \mathcal{H}_B$ consists of two copies of the original Hilbert space, which we denote as the physical Hilbert space $\mathcal{H}_P$ and the bath Hilbert space $\mathcal{H}_B$ (see first arrow in Fig. 2). Correspondingly, we denote the density operators $\hat{n}_{P;j}$ and $\hat{n}_{B;j}$, which have exactly the same properties as the density operators $\hat{n}_j$ in the original Hilbert space. In particular, the basis states $|n_{P/B;1}\rangle \otimes \cdots \otimes |n_{P/B;L}\rangle \equiv |n_{P/B;1} \cdots n_{P/B;L}\rangle$ span a complete orthonormal basis of $\mathcal{H}_{P/B}$.

Here, we leave the framework of finite-temperature DMRG by considering the subspace $\mathcal{P} \subset \mathcal{H}_{PB} = \mathcal{H}_P \otimes \mathcal{H}_B$ of the doubled system that is spanned by all states

$$|n_{P;1}, \ldots, n_{P;L}) = |n_{P;1}, \ldots, n_{P;L}\rangle_P \otimes |g(n_{P;1}), \ldots, g(n_{P;L})\rangle_B \tag{9}$$

$$= |n_{P;1}, \ldots, n_{P;L}, g(n_{P;1}), \ldots, g(n_{P;L})\rangle_{PB} \,, \tag{10}$$

with $n_{P;j} \in [0, \sigma - 1]$ and $g(x) = \sigma - 1 - x$ (see second arrow in Fig. 2). Note that for convenience we have labeled the kets in the physical and bath system by subscripts and introduced rounded kets to indicate states in the subspace $\mathcal{P} \subset \mathcal{H}_{PB}$, which depend only on a reduced number of coefficients $n_{P;1}, \ldots, n_{P;L}$. This subspace is contained in the subspace with $N_P + N_B = (\sigma - 1) \cdot L$, i.e.,

$$(\hat{N}_P + \hat{N}_B) |n_{P;1}, \ldots, n_{P;L}) = (\sigma - 1) \cdot L |n_{P;1}, \ldots, n_{P;L}) \,, \tag{11}$$

so that all states in the subspace $\mathcal{P}$ transform symmetrically under the action of the global $U(1)$ symmetry generated by $\hat{N}_P + \hat{N}_B$. Furthermore, note that by counting the number of basis states spanning $\mathcal{P}$ it follows that $\dim \mathcal{H} = \dim \mathcal{P}$.

Now, we define the map

$$I : \mathcal{P} \longrightarrow \mathcal{H}$$
$$|\psi) \longmapsto |\psi\rangle \,, \tag{12}$$

identifying states $|\psi) \in \mathcal{P}$ in the subspace of the doubled system with states $|\psi\rangle \in \mathcal{H}$ in the original Hilbert space as shown in Fig. 2. Since $g(x)$ is invertible and $\dim \mathcal{P} = \dim \mathcal{H}_P = \dim \mathcal{H}$, it follows that I is invertible. Next, we define the projected purified operator $\hat{O}_{PP} : \mathcal{P} \longrightarrow \mathcal{P}$ by

$$\hat{O} = I \hat{O}_{PP} I^{-1} \,. \tag{13}$$

Assuming $\hat{O}_{PP}$ exists, this definition implies in particular that

$$\langle n_1, \ldots, n_L | \hat{O} | n'_1, \ldots, n'_L \rangle = (n_{P;1}, \ldots, n_{P;L} | \hat{O}_{PP} | n'_{P;1}, \ldots, n'_{P;L}) \,, \tag{14}$$

that is, the matrix representations of $\hat{O}$ and $\hat{O}_{PP}$ in the local basis sets $\{|n_1, \ldots, n_L\rangle\}$ and $\{|n_{P;1}, \ldots, n_{P;L}\rangle\}$ are identical. We can, hence, work with $\hat{O}_{PP}$ in the subspace $\mathcal{P}$ instead of $\hat{O}$. In order to show that $\hat{O}_{PP}$ always exists, we construct it explicitly. For that purpose, we note that the above definition of $\mathcal{P}$ is equivalent to

$$|\psi) \in \mathcal{P} \Leftrightarrow (\hat{n}_{P;j} + \hat{n}_{B;j}) |\psi) = (\sigma - 1) |\psi) \quad \text{for all } j \in \{1, \ldots, L\} \,. \tag{15}$$

But this means that each operator $\hat{O}_{PP}$ has to satisfy

$$\left[\hat{O}_{PP}, \hat{n}_{P;j} + \hat{n}_{B;j} \right] = 0 \quad \text{for all } j \in \{1, \ldots, L\} \,. \tag{16}$$

This motivates us to define balancing operators $\hat{\beta}_{B;j} / \hat{\beta}^{\dagger}_{B;j} : \mathcal{H}_{B,\sigma} \longrightarrow \mathcal{H}_{B,\sigma}$

$$_B\langle n'_{B;j} | \hat{\beta}_{B;j} | n_{B;j} \rangle_B = \delta_{n'_{B;j}, n_{B;j}+1} \tag{17}$$

$$_B\langle n'_{B;j} | \hat{\beta}^{\dagger}_{B;j} | n_{B;j} \rangle_B = \delta_{n'_{B;j}, n_{B;j}-1} \tag{18}$$

$$\left[\hat{\beta}^{(\dagger)}_{B;j}, \hat{b}^{(\dagger)}_{P;k} \right] = 0 \,. \tag{19}$$

Since every operator $\hat{O}_P \otimes \hat{\mathbf{1}}_B$ acting non-trivially only on $\mathcal{H}_P$ can be expressed as function of a product of ladder operators $\hat{b}^{[\dagger]}_{P,j}$, we can thus map it to $\mathcal{P}$ through the transformations

$$\hat{b}^{\dagger}_{P;j} \longrightarrow \hat{b}^{\dagger}_{P;j} \hat{\beta}_{B;j} \quad \text{and} \quad \hat{b}_{P;j} \longrightarrow \hat{b}_{P;j} \hat{\beta}^{\dagger}_{B;j} \,, \tag{20}$$

and imposing the local gauge fixing conditions Eq. (15). By means of this transformation, which is shown graphically in Fig. 1, the local conservation laws Eq. (16) are fulfilled.

There is also another way to introduce projected purified operators. We can define the projection operator

$$\hat{P} = \sum_{\{n_{P;j}\}} |n_{P;1}, \ldots, n_{P;L}) (n_{P;1}, \ldots, n_{P;L}| \tag{21}$$

and look for operators satisfying $\hat{P} \hat{O}_{PP} \hat{P} = \hat{O}_{PP}$. Those operators are manifestly invariant under a projection into $\mathcal{P}$ and therefore, ignoring zero elements, have the same matrix elements in both $\mathcal{H}$ and $\mathcal{P}$. Here the important observation is that restricting the ansatz class of states $|\psi\rangle_{PB} \in \mathcal{H}_{PB}$ to $\mathcal{P}$, we have found a one-to-one mapping between $\mathcal{H}$ and $\mathcal{P} \subset \mathcal{H}_{PB}$, and the states $|\psi) = \hat{P} |\psi\rangle_{PB}$ transform under the global $U(1)$ symmetry generated by $\hat{N}_P + \hat{N}_B$, obeying Eq. (15).

In the following, we explicitly derive the representation of states in $\mathcal{P}$ in terms of MPS and demonstrate the capability of the introduced $U(1)$ symmetrization to improve the numerical efficiency of MPS calculations. For that purpose, we briefly recapitulate $U(1)$-invariant MPS before digging into the technical details of the projection.
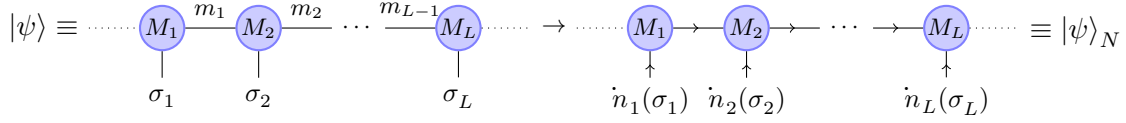
Figure 3: Schematic of the tensor network of a MPS. Horizontal lines denote the internal indices with bond dimension m_j, whereas the vertical lines denote physical indices with dimension d. Dotted lines to the left and right indicate the dummy indices m_0 and m_L.

4 $U(1)$ Symmetries in Matrix-Product States

Consider a state $|\psi\rangle$ as described in Eq. (7). Within the MPS formulation [31], the coefficients $\psi_{\sigma_1 \dots \sigma_L}$ are expanded into a tensor train of rank-3 tensors $M^{\sigma_j}_{j;m_{j-1},m_j}$. For each lattice site j, there is a set of σ matrices $M^{\sigma_j}_j \in \mathbb{C}^{m_{j-1} \times m_j}$. We refer to the matrix dimensions m_j as bond dimensions. A compact representation of $|\psi\rangle$ is then given by

$$|\psi\rangle = \sum_{\sigma_1, \dots, \sigma_L} \underbrace{M^{\sigma_1}_1 \cdots M^{\sigma_L}_L}_{\psi_{\sigma_1 \dots \sigma_L}} |\sigma_1 \cdots \sigma_L\rangle \ , \tag{22}$$

where neighboring matrices are contracted over their shared bond indices: $M^{\sigma_j} M^{\sigma_{j+1}} = \sum_{m_j} M^{\sigma_j}_{j;m_{j-1},m_j} M^{\sigma_{j+1}}_{j+1;m_j,m_{j+1}}$. Commonly, these contractions are represented pictographically. Each tensor is drawn as a shape with as many legs attached to it as there are indices. Then, contractions over shared indices are indicated by connecting the corresponding legs as shown in Fig. 3 for the case of a MPS.

In order to exploit $U(1)$ symmetries, let us consider a Hamilton operator $\hat{H} : \mathcal{H} \longrightarrow \mathcal{H}$ of a system and $\hat{N} : \mathcal{H} \longrightarrow \mathcal{H}$ an operator generating a global $U(1)$ symmetry of $\hat{H}$, i.e.,

$$\left[\hat{H}, \hat{N}\right] = 0, \quad \hat{N} = \sum_{j=1}^{L} \hat{n}_j, \quad [\hat{n}_j, \hat{n}_k] = 0 \tag{23}$$

with local density operators $\hat{n}_j : \mathcal{H}_\sigma \longrightarrow \mathcal{H}_\sigma$ acting only on the jth lattice site.

Since $[\hat{H}, \hat{N}] = 0$, we can diagonalize both operators $\hat{H}$ and $\hat{N}$ in the same basis. Let this basis be spanned by $\{|N\rangle\}$ with $\hat{N}|N\rangle = N|N\rangle$ as well as $\langle N|N'\rangle = \delta_{N,N'}$. N is called the global quantum number of the state $|N\rangle$. A state $|\psi\rangle \in \mathcal{H}$ can now be expanded in terms of the simultaneous eigenstates $|n_1, \dots, n_L\rangle \in \mathcal{H}$ of $\hat{N}$ with $N = \sum_j n_j$ and labels n_j denoting the eigenvalues of the local operators[3] $\hat{n}_j$:

$$|\psi\rangle = \sum_{n_1, \dots, n_L} \psi_{n_1 \cdots n_L} |n_1, \dots, n_L\rangle = \sum_{n_1, \dots, n_L} M^{n_1}_1 \cdots M^{n_L}_L |n_1, \dots, n_L\rangle \ , \tag{24}$$

As a consequence of the Wigner-Eckart theorem, it can be shown [35, 36] that the site tensors decompose according to

$$\left(M^{n_j}_{j;\alpha_{j-1},\alpha_j}\right)_{m_{j-1};\alpha_{j-1},m_j;\alpha_j} = M^{n_j}_{j;\underbrace{\alpha_{j-1},m_{j-1};\alpha_{j-1}}_{\pi_{j-1}},\underbrace{\alpha_j,m_j;\alpha_j}_{\pi_j}} = T^{n_j}_{j;\pi_{j-1},\pi_j} \cdot S^{n_j}_{j;\alpha_{j-1},\alpha_j} \tag{25}$$

---

[3]If the local operators have degenerated eigenvalues, more labels have to be used as a set to identify each state uniquely.
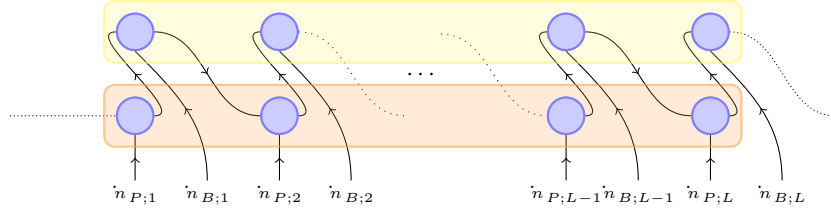
Figure 4: MPS representation in an enlarged Hilbert space with each physical site accompanied by a bath site.
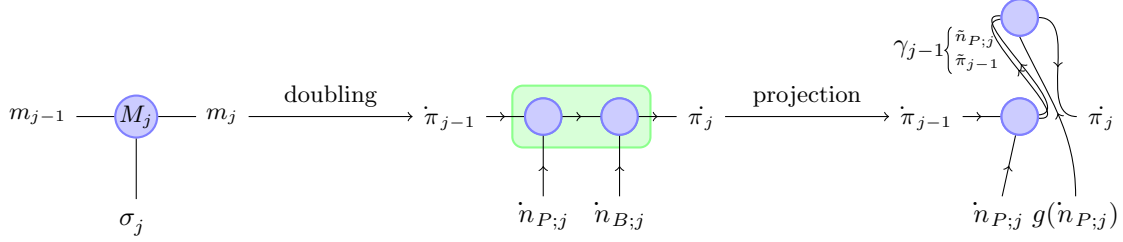
Figure 5: Decomposition of general MPS tensor (left) into $U(1)$-invariant physical and bath-site tensors (center). Projection of the $U(1)$-invariant MPS (center) into the subspace $\mathcal{P}$ (right) enforcing the local gauge condition given in Eq. (15). Decomposition of the introduced auxiliary index $\tilde{\pi}_{j-1}$ into irreducible representation of the local conservation law generated by $\hat{n}_{P;j} + \hat{n}_{B;j}$ is sketched by double bonds $\gamma_{j-1} \to (\tilde{n}_{P;j}, \tilde{\pi}_{j-1})$.

with

$$S^{\dot{n}_j}_{j;\dot{\alpha}_{j-1},\dot{\alpha}_j} = \delta(\dot{n}_j + \dot{\alpha}_{j-1} - \dot{\alpha}_j) \,, \tag{26}$$

where we interpret in the following

$$T^{\dot{n}_j}_{j;\dot{\pi}_{j-1},\dot{\pi}_j} = \left(T^{\dot{n}_j}_{j;\dot{\alpha}_{j-1},\dot{\alpha}_j}\right)_{m_{j-1;\dot{\alpha}_{j-1}},m_{j;\dot{\alpha}_j}} \,, \quad \text{hence} \quad T^{\dot{n}_j}_{j;\dot{\alpha}_{j-1},\dot{\alpha}_j} \in \mathbb{C}^{m_{j-1;\dot{\alpha}_{j-1}} \times m_{j;\dot{\alpha}_j}} \,. \tag{27}$$

Here, the indices $\dot{\alpha}_{j-1}, \dot{\alpha}_j$ are labeling irreducible representations of the $U(1)$ symmetry on the bond spaces. Note that we introduce a dot over an index shifted towards the tensor $\dot{\pi}_j$ to indicate an ingoing index and a dot over an index shifted away from the tensor $\pi_{\dot{j}}$ to indicate an outgoing index. The orientation of the bond indices is also shown in Fig. 3. Hence, we can describe a state by its rank-5 site tensors $M^{\dot{n}_j}_{j;\dot{\pi}_{j-1},\pi_{\dot{j}}}$ and benefit from their block structure. The matrices $M^{\dot{n}_j}_j$ are decomposed into blocks $T^{\dot{n}_j}_{j;\dot{\alpha}_{j-1},\dot{\alpha}_j}$ with overall dimensions $m_j = \sum_{\alpha_j} m_{j;\dot{\alpha}_j}$. However, matrix multiplications only scale with the block bond dimensions $m_{j;\dot{\alpha}_j}$ and are thus cheaper by a factor of $\left(\frac{m_j}{m_{j;\dot{\alpha}_j}}\right)^3$, i.e., typically $\sim \mathcal{O}(10) - \mathcal{O}(100)$.

5 $U(1)$-Invariant Matrix-Product States with Bath Sites

The introduced mapping from an operator breaking a global $U(1)$ symmetry to one conserving a $U(1)$ symmetry (see Sec. 3) can be exploited to efficiently reduce the matrix sizes of MPS representations. The key observation is that, while purified states in the doubled

Hilbert space in general have a huge redundancy that comes with additional gauge degrees of freedom, the projection into $\mathcal{P}$ fixes all these gauge degrees of freedom by the L local gauge constraints given in Eq. (15). Here, we discuss the implications on the projection of purified MPS into $\mathcal{P}$ and derive an important connection between the Schmidt decomposition of the purified states and the single-site reduced density matrix.

Let again $|\psi\rangle \in \mathcal{H}$ and consider its single-site representation

$$|\psi\rangle = \sum_{m_{j-1}, m_j, n_j} M^{n_j}_{j; m_{j-1}, m_j} |m_{j-1}\rangle \otimes |n_j\rangle \otimes |m_j\rangle \ , \tag{28}$$

with $\langle m_{j-1}|m'_{j-1}\rangle = \delta_{m_{j-1}, m'_{j-1}}$ and $\langle m_j|m'_j\rangle = \delta_{m_j, m'_j}$. Following the previous considerations, we take this state representation into the subspace $\mathcal{P}$ of the enlarged Hilbert space $\mathcal{H}_{PB}$ with $N_P + N_B = (\sigma - 1) \cdot L$. We represent the MPS in $\mathcal{H}_{PB}$ by interpreting the single-site representation of $|\psi\rangle$ as a two-site representation in $\mathcal{H}_{PB}$,

$$|\psi\rangle_{PB} = \sum_{\substack{\dot{\pi}_{j-1}, \dot{\pi}_j \\ \dot{n}_{P;j}, \dot{n}_{B;j}}} M^{\dot{n}_{P;j}, \dot{n}_{B;j}}_{j; \dot{\pi}_{j-1}, \dot{\pi}_j} |\dot{\pi}_{j-1}\rangle \otimes |\dot{n}_{P;j}, \dot{n}_{B;j}\rangle_{PB} \otimes |\dot{\pi}_j\rangle \ . \tag{29}$$

Then, we apply the projection into the subspace $\mathcal{P}$ by enforcing the local gauge condition Eq. (15). Pursuing those two steps at all sites $j \in \{1, \ldots, L\}$, the resulting state representation is in the subspace $\mathcal{P}$ of the enlarged Hilbert space $\mathcal{H}_{PB}$

$$|\psi\rangle = \sum_{\substack{\dot{\pi}_{j-1}, \dot{\pi}_j \\ \dot{n}_{P;j}, \dot{n}_{B;j}}} M^{\dot{n}_{P;j}, \dot{n}_{B;j}}_{j; \dot{\pi}_{j-1}, \dot{\pi}_j} \delta_{\dot{n}_{B;j}, g(\dot{n}_{P;j})} |\dot{\pi}_{j-1}\rangle \otimes |\dot{n}_{P;j}, \dot{n}_{B;j}\rangle_{PB} \otimes |\dot{\pi}_j\rangle \ . \tag{30}$$

The resulting site tensors decompose under the global $U(1)$ symmetry as

$$M^{\dot{n}_{P;j}, \dot{n}_{B;j}}_{j; \dot{\pi}_{j-1}, \dot{\pi}_j} = T^{\dot{n}_{P;j}, \dot{n}_{B;j}}_{j; \dot{\alpha}_{j-1}, \dot{\alpha}_j} \delta(\dot{n}_{P;j} + \dot{n}_{B;j} + \dot{\alpha}_{j-1} - \dot{\alpha}_j) \ . \tag{31}$$

A matrix factorization of the decomposed site tensors $M^{\dot{n}_{P;j}, \dot{n}_{B;j}}_j = \bigoplus_{N_j} T^{\dot{n}_{P;j}, \dot{n}_{B;j}}_{j; N_j}$ in each symmetry block $\dot{n}_{P;j} + \dot{\alpha}_{j-1} = N_j = \dot{n}_{B;j} + \dot{\alpha}_j$ yields the MPS representation of $|\psi\rangle$ in the subspace $\mathcal{P}$ of the enlarged Hilbert space

$$|\psi\rangle = \sum_{\dot{\pi}_{j-1}, \dot{\gamma}_{j-1}, \dot{n}_{P;j}} T^{\dot{n}_{P;j}}_{j; \dot{\alpha}_{j-1}, \dot{\gamma}_{j-1}} \delta(\dot{n}_{P;j} + \dot{\alpha}_{j-1} - \dot{\gamma}_{j-1}) |\dot{\pi}_{j-1}\rangle \otimes |\dot{n}_{P;j}\rangle \times$$

$$\sum_{\dot{\pi}_j, \dot{n}_{B;j}} T^{\dot{n}_{B;j}}_{j; \dot{\gamma}_{j-1}, \dot{\alpha}_j} \delta(\dot{n}_{B;j} + \dot{\gamma}_{j-1} - \dot{\alpha}_j) \delta_{\dot{n}_{B;j}, g(\dot{n}_{P;j})} |\dot{n}_{B;j}\rangle \otimes |\dot{\pi}_j\rangle \ . \tag{32}$$

The MPS constructed in this way is shown in Fig. 4 and consists of alternating physical and bath sites, which are labeled by the physical and bath degrees of freedom $n_{P;j}$ and $n_{B;j}$, respectively. The delta function $\delta_{\dot{n}_{B;j}, g(\dot{n}_{P;j})}$ in the last line of Eq. (32) is again the manifestation of the L gauge-fixing conditions imposed in Eq. (15). It motivates the introduction of the auxiliary bond labels η_j enumerating the irreducible representations of each locally conserved quantity between the physical and bath sites. In this way the bond label γ_{j-1} can be decomposed into labels $\gamma_{j-1} \to (\eta_j, a_{j-1})$ that need to fulfill $\eta_j + a_{j-1} = n_{P;j} + \alpha_{j-1}$. Note that we focus only on the labels for the symmetry blocks and – for convenience – in the following neglect the bond dimension m, which is part of the label π. From the local conservation laws and the gauge fixing, we can furthermore

conclude that the bond label a_{j-1} has only one non-vanishing block with respect to the global $U(1)$ symmetry, which is characterized by a quantum number $(j-1)\cdot(\sigma-1) \equiv \alpha_{j-1}$. Accordingly, there is only one non-vanishing block α_j to the right of the bath site, which is characterized by a quantum number $j \cdot (\sigma - 1) \equiv \alpha_j$. In tensor notation, this can be expressed by a reformulation of the local conservation laws at every site, introducing for brevity $N_j = (\sigma - 1) \cdot (j - 1)$,

$$\sum_{\gamma_j} T^{n_{P;j}}_{j;\alpha_{j-1},\gamma_{j-1}} T^{n_{B;j}}_{j;\gamma_{j-1},\alpha_j} \delta_{n_{B;j},g(n_{P;j})}$$

$$= \sum_{\eta_j,a_{j-1}} T^{n_{P;j}}_{j;\alpha_{j-1},(\eta_j,a_{j-1})} \delta(N_j - \alpha_{j-1}) T^{n_{B;j}}_{j;(\eta_j,a_{j-1}),\alpha_j} \delta(N_{j+1} - \alpha_j) \delta_{n_{B;j},g(n_{P;j})} \, . \tag{33}$$

Therefore, we find that there is a unique decomposition of the auxiliary bond label $\gamma_{j-1} = (\eta_j, a_{j-1})$ given by identifying $\eta_j \equiv n_{P;j}$ and thus also $a_{j-1} \equiv \alpha_{j-1}$. This can be summarized by decomposing the site tensors as

$$\sum_{\gamma_j} T^{n_{P;j}}_{j;\alpha_{j-1},\gamma_{j-1}} T^{n_{B;j}}_{j;\gamma_{j-1},\alpha_j} \delta_{n_{B;j},g(n_{P;j})}$$

$$= \sum_{\tilde{n}_{P;j},\tilde{\alpha}_{j-1}} T^{n_{P;j}}_{j;\alpha_{j-1},(\tilde{\alpha}_{j-1}\tilde{n}_{P;j})} T^{n_{B;j}}_{j;(\tilde{\alpha}_{j-1}\tilde{n}_{P;j}),\alpha_j} \delta_{\alpha_{j-1},\tilde{\alpha}_{j-1}} \delta_{n_{P;j},\tilde{n}_{P;j}} \delta_{n_{B;j},g(n_{P;j})} \, , \tag{34}$$

which is exemplary shown in Fig. 5 and presumed from now on.

5.1 Connection to single-site reduced density matrix

The projected purification introduced above is closely related to the single-site reduced density matrix, which is the central object of the LBO method [13, 40, 42]. We consider the expectation value of the local density operators in the original Hilbert space written in terms of the single-site reduced density matrix $\hat{\rho}_j = \mathrm{Tr}_{k \neq j} \, \hat{\rho}$,

$$\langle \hat{n}_j \rangle = \mathrm{Tr}_j \left\{ \hat{\rho}_j \hat{n}_j \right\} = \sum_{n_j} \langle n_j | \hat{\rho}_j \hat{n}_j | n_j \rangle = \sum_{n_j} \rho_{n_j,n_j} n_j \, . \tag{35}$$

Expanding the expectation value of $\hat{n}_{P;j}$ in terms of the physical system's single-site reduced density matrix $\hat{\rho}_{P;j}$ for states $|\psi\rangle \in \mathcal{P}$ and a mixed-canonical MPS with center of orthogonality at the physical site j yields

$$(\hat{n}_{P;j}) = \mathrm{Tr}_{P;j} \left\{ \hat{\rho}_{P;j} \hat{n}_{P;j} \right\} = \sum_{n_{P;j}} (n_{P;j} | \hat{\rho}_{P;j} \hat{n}_{P;j} | n_{P;j}) = \sum_{n_{P;j}} \rho_{n_{P;j},n_{P;j}} n_{P;j} \tag{36}$$

$$= \sum_{\substack{n_{P;j},n'_{P;j}, \\ \tilde{n}_{P;j},\tilde{\alpha}_{j-1}, \\ \alpha_{j-1}}} n_{P;j} \left(T^{n'_{P;j}}_{j;\alpha_{j-1},(\tilde{n}_{P;j},\tilde{\alpha}_{j-1})} \delta_{n'_{P;j},\tilde{n}_{P;j}} \right)^* T^{n_{P;j}}_{j;\alpha_{j-1},(\tilde{n}_{P;j},\tilde{\alpha}_{j-1})} \delta_{n_{P;j},\tilde{n}_{P;j}}$$

$$= \sum_{n_{P;j}} n_{P;j} \sum_{\substack{\tilde{n}_{P;j},\tilde{\alpha}_{j-1}, \\ \alpha_{j-1}}} \left| T^{n_{P;j}}_{j;\alpha_{j-1},(\tilde{n}_{P;j},\tilde{\alpha}_{j-1})} \delta_{n_{P;j},\tilde{n}_{P;j}} \right|^2 \, , \tag{37}$$

where we made use of the fact that the local symmetry generators $\hat{n}_{P;j}$ are one-dimensional representations of the local $U(1)$ symmetry (see Fig. 6). From Eq. (14) it follows that Eq. (36) and Eq. (35) are completely equivalent so that

$$\rho_{n_j,n_j} = \rho_{n_{P;j},n_{P;j}} \, , \tag{38}$$
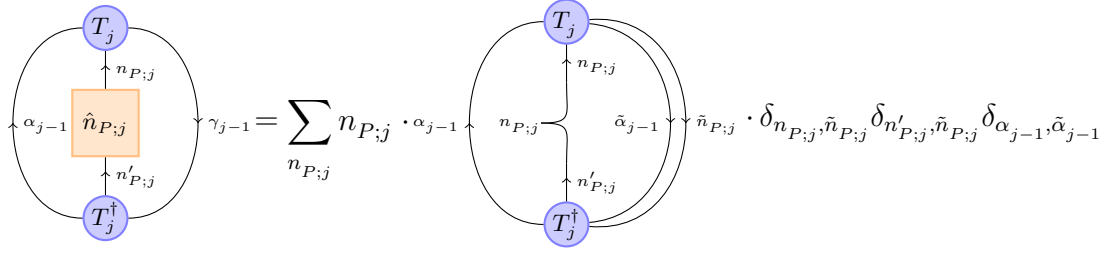
Figure 6: Expectation value of the local density $\langle \hat{n}_{P;j} \rangle$, which by Eq. (39) can be directly related to the diagonal elements of the reduced single-site density matrix in the eigenbasis $\hat{n}_{P;j}$.

and thus, comparing to Eq. (37),

$$\rho_{n_j, n_j} = \left| T^{\dot{n}_{P;j}}_{j;\dot{\alpha}_{j-1},(\dot{\tilde{n}}_{P;j},\dot{\tilde{\alpha}}_{j-1})} \delta_{n_{P;j},\tilde{n}_{P;j}} \right|^2 . \tag{39}$$

We hence find that the single-site reduced density matrix of the physical part of $\mathcal{P}$ has the same diagonal elements as the original one. They are given by the trace over the absolute square of the symmetry blocks of the mixed-canonical site tensors. However, the symmetry conservation in $\mathcal{P}$ implies that $\hat{\rho}_{P;j}$ is diagonal whereas $\hat{\rho}_j$ in general is not. We can write the distance with respect to the 1-norm of these two operators by means of the mapping I:

$$\|\hat{\rho}_j - I\hat{\rho}_{P;j}I^{-1}\|_1 = \mathrm{Tr}_j\left\{\hat{\rho}_j\right\} - \mathrm{Tr}_j\left\{\hat{I}\rho_{P;j}I^{-1}\right\}$$
$$= \mathrm{Tr}_j\left\{\hat{\rho}_j\right\} - \sum_{n_{P;j}} \left| T^{\dot{n}_{P;j}}_{j;\dot{\alpha}_{j-1},(\dot{\tilde{n}}_{P;j},\dot{\tilde{\alpha}}_{j-1})} \delta_{n_{P;j},\tilde{n}_{P;j}} \right|^2 . \tag{40}$$

Here, we link to the LBO method, which expresses $\hat{\rho}_j$ in its eigenbasis (optimal modes) with diagonal elements w_{n_j} so that

$$\|\hat{\rho}_j - I\hat{\rho}_{P;j}I^{-1}\|_1 = \sum_{n_j} w_{n_j} - \sum_{n_{P;j}} \left| T^{\dot{n}_{P;j}}_{j;\dot{\alpha}_{j-1},(\dot{\tilde{n}}_{P;j},\dot{\tilde{\alpha}}_{j-1})} \delta_{n_{P;j},\tilde{n}_{P;j}} \right|^2 . \tag{41}$$

Let us now consider the Schmidt decomposition of a state $|\psi\rangle$ at the auxiliary bond $\gamma_{j-1} = (\tilde{n}_{P;j}, \tilde{\alpha}_{j-1})$. Because α_j is fixed for every j, a block for a given $n_{P;j}$ of a physical site can be decomposed individually to

$$T^{\dot{n}_{P;j}}_{j;\dot{\alpha}_{j-1},\dot{\gamma}_{j-1}} = U^{\dot{n}_{P;j}}_{j;\dot{\alpha}_{j-1},\dot{\bar{\gamma}}_{j-1}} \Lambda_{j;\dot{\bar{\gamma}}_{j-1},\dot{\bar{\bar{\gamma}}}_{j-1}} V_{j;\dot{\bar{\bar{\gamma}}}_{j-1},\dot{\gamma}_{j-1}} \delta_{\bar{\bar{\gamma}}_{j-1},\tilde{\gamma}_{j-1}} \delta_{\tilde{\gamma}_{j-1},\gamma_{j-1}} . \tag{42}$$

The sum over the squared singular values is identified with the corresponding (diagonal) entry of the single-site reduced density matrix

$$\sum_{\tau} \left(\Lambda_{j;\dot{\gamma}_{j-1},\tau,\dot{\bar{\gamma}}_{j-1},\tau} \right)^2 = \rho_{n_{P;j},n_{P;j}} . \tag{43}$$

Note that we implicitly accounted for all constraints arising from the projection into $\mathcal{P}$ and wrote the γ_{j-1} on the left only for completeness, as all α are fixed and the $n_{P;j}$ is chosen. In Fig. 7, the argument is given diagrammatically.
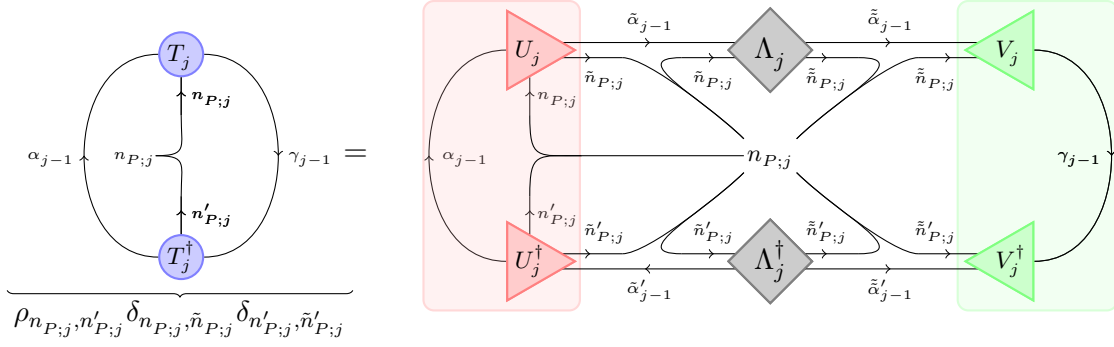
Figure 7: For a given $n_{P;j}$, the diagonal entry of the single-site reduced density matrix is given by the singular values of the decomposed physical site. Note that we make extensive use of the tensor notation, in particular implicit deltas, which was introduced in [47].

Truncating the singular values according to a certain threshold $0 < \delta \ll 1$, so that $\sum_{n_{P;j}} \sum_\tau \left(\Lambda_{j;\tau}^{n_{P;j}} \right)^2 < 1 - \delta$ implies a rescaling of the diagonal elements of the single-site reduced density matrix $(n_{P;j}|\hat{\rho}_{P;j}|n_{P;j})$, which is governed by the decay of the singular values $\Lambda_{j,\tau}^{n_{P;j}}$ in each block. If we assume that the optimal modes of $\hat{\rho}_j$ are truncated in the same way, so that $\sum_{n_j} w_{n_j} < 1 - \delta$, we can compare this expression with Eq. (41). Then, using the invariance of the trace, a truncation of the bond index γ_{j-1} by means of the usual MPS truncation routine yields an equivalently precise approximation to $\hat{\rho}_j$ as the truncation occurring in the LBO. In addition, performing the truncation in the projected purified representation automatically favors those eigenvalues of $\hat{\rho}_j$ that have the largest weight without the necessity of constructing the single-site reduced density matrix at all. This is an important improvement as it prevents the repeated constructions of $\hat{\rho}_j$ in contrast to the LBO.

5.2 Characterization of numerical expenses

The previous considerations enable us to compare the numerical complexity of typical tensor contractions arising from the MPS representation of states $|\psi\rangle \in \mathcal{P}$ with those of MPS representations without the expansion of the Hilbert space. At first, we point out again that due to the local conservation laws and the gauge fixing, the bond labels α_{j-1}, α_j of the MPS site tensors $T_{j;\alpha_{j-1},\gamma_{j-1}}^{n_{P;j}}$ and $T_{j;\gamma_{j-1},\alpha_j}^{n_{B;j}}$ have only one non-vanishing entry; each of which is given by $\alpha_{j-1} = N_j, \alpha_j = N_{j+1}$ with N_j as defined above. Therefore, without truncation, the bond dimensions m_{j-1}, m_j are identical to those of the site tensors $M_{j;\alpha_{j-1},\alpha_j}^{n_j}$ representing the same state in the physical Hilbert space $\mathcal{H}$ only. There is no additional complexity arising from the representation of $|\psi\rangle \in \mathcal{P}$ on these indices. Furthermore, without truncation the effective bond dimensions on the γ-bonds are given by $m_{j;\gamma} = n_{P;j} \cdot \min(m_{j-1}, m_j)$. In what follows, we analyze two truncation schemes on these bonds for states in the enlarged Hilbert space $\mathcal{H}_{PB}$. Thereafter, we discuss in which situations these yield a reduced numerical complexity of the most expensive operation during ground-state calculations, i.e., the application of a matrix-product operator (MPO) to a state.

A physically motivated truncation can be defined by exploiting Eq. (43) and discarding all single-site occupations of $\hat{\rho}_j$, whose sum is below a given threshold $\delta > 0$. More precisely, let $\mathcal{D} \subset \left\{0, \cdots, n_{P;j} - 1\right\}$ be a set for which $\sum_{n_{P;j} \in \mathcal{D}} \rho_{n_{P;j}} < 1 - \delta$. Since $\hat{\rho}_j$

is a reduced density matrix, its trace is normalized, and by sorting the diagonal elements such a set can always be defined. Then, all tensor blocks $T^{\dot{n}_{P;j}}_{j;\dot{\alpha}_{j-1},\tilde{\alpha}_{j-1}\tilde{n}_{P;j}}$ with $n_{P;j} \notin \mathcal{D}$ are discarded so that the total number of kept states on the auxiliary bond is bounded by $m_{j;\gamma} \leq |\mathcal{D}| \min(m_{j-1}, m_j)$. The physical interpretation is straightforward: All tensor blocks $T^{\dot{n}_{P;j}}$ that have a negligible single-site occupation $\left|T^{\dot{n}_{P;j}}\right|^2 = \hat{\rho}_{n_{P;j}}$ are discarded, i.e., empty modes do not contribute to the physics. However, we can give a tighter estimate by considering the explicit distribution of the singular values in each block.

Motivated by the numerical evidence that often the singular values decay exponentially in ground states of one-dimensional (1D) gaped systems [25,29,39], we assume such a decay in each block $T^{\dot{n}_{P;j}}_{j;\dot{\alpha}_{j-1},\tilde{\alpha}_{j-1}\tilde{n}_{P;j}}$ $(n_{P;j} \in \mathcal{D})$. That means, in the decomposition shown in Fig. 7,

$$\Lambda^{n_{P;j}}_{j;\tau} = e^{-a_{n_{P;j}}\tau}, \quad \sum_{\tau=1}^{m_j} e^{-2a_{n_{P;j}}\tau} = \rho_{n_{P;j}} , \tag{44}$$

for some $a_{n_{P;j}} > 0$ and we abbreviated $m_j \equiv \min(m_{j-1}, m_j)$. Note that $n_{P;j}$ only specifies one block (due to the implicit $\delta_{n_{P;j},\tilde{n}_{P;j}}$) and that we neglected the constant α_j for brevity. Normalization to the single-site occupation yields

$$\rho_{n_{P;j}} = e^{-2a_{n_{P;j}}} \sum_{\tau=0}^{m_j-1} \left(e^{-2a_{n_{P;j}}} \right)^\tau = \frac{e^{-2a_{n_{P;j}}} - e^{-2a_{n_{P;j}}(m_j+1)}}{1 - e^{-2a_{n_{P;j}}}} . \tag{45}$$

Defining $a_{n_{P;j}} = -\frac{1}{2}\log X_{n_{P;j}}$ with $0 < X_{n_{P;j}} < 1$, we can rewrite Eq. (45) into

$$X^{m_j+1}_{n_{P;j}} = X_{n_{P;j}}(1 + \rho_{n_{P;j}}) - \rho_{n_{P;j}} . \tag{46}$$

Since $\delta \leq \rho_{n_{P;j}} \leq 1$ and $m_j \geq 1$, this equation has only one solution for $X_{n_{P;j}}$ in the given domain, even though there is no closed expression (see Fig. 8 for graphical solution at distinct pairs $(\rho_{n_{P;j}}, m_j)$). Therefore, we consider two limiting cases that yield upper and lower bounds on the decay of the singular values in each tensor block. The lower bound $X_{n_{P;j},\min}$ is obtained through the intersection of the right-hand side with the horizontal axis and can be related to the limit $m_j \gg 1$:

$$0 = X_{n_{P;j},\min}(1 + \rho_{n_{P;j}}) - \rho_{n_{P;j}}$$
$$\Rightarrow X_{n_{P;j}} \geq X_{n_{P;j},\min} = \frac{\rho_{n_{P;j}}}{1 + \rho_{n_{P;j}}} . \tag{47}$$

An upper bound $X_{n_{P;j},\max}$ can be established if the right-hand side of Eq. (46) is tangential to the left-hand side

$$\frac{d}{dX_{n_{P;j}}} X^{m_j+1}_{n_{P;j}} \bigg|_{X_{n_{P;j},\max}} \overset{!}{=} 1 + \rho_{n_{P;j}}$$
$$\Rightarrow X_{n_{P;j}} \leq X_{n_{P;j},\max} = \left(\frac{1 + \rho_{n_{P;j}}}{1 + m_j} \right)^{1/m_j} . \tag{48}$$

Combining both bounds, we find

$$-\frac{1}{2m_{n_{P;j}}} \log \frac{1 + \rho_{n_{P;j}}}{1 + m_j} \leq a_{n_{P;j}} \leq -\frac{1}{2} \log \frac{\rho_{n_{P;j}}}{1 + \rho_{n_{P;j}}} , \tag{49}$$
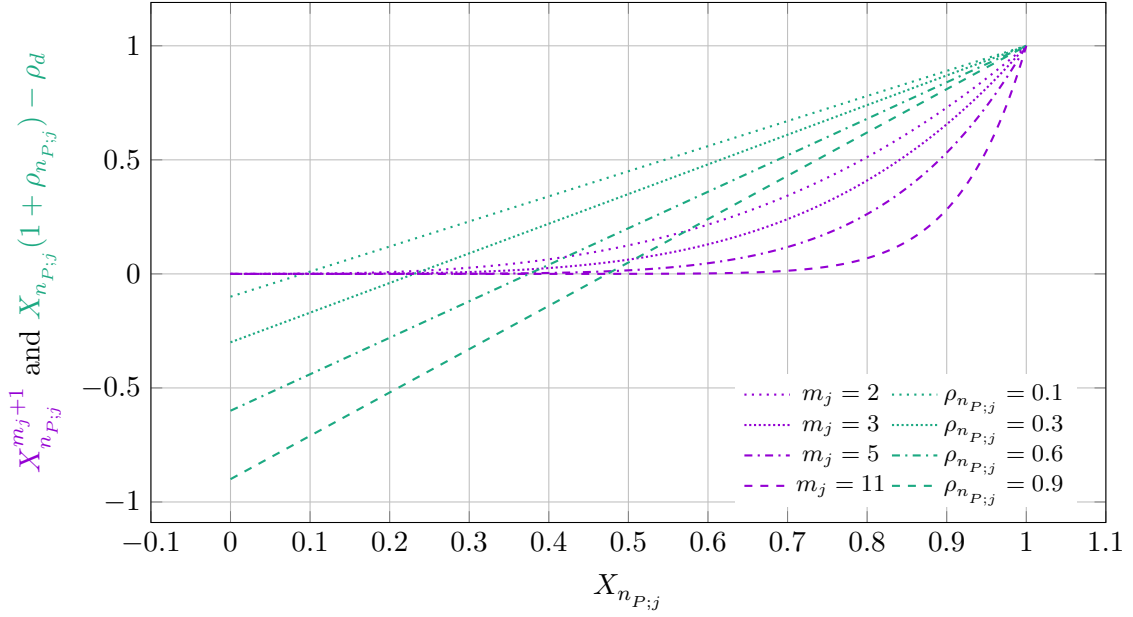
Figure 8: Left (purple) and right (green) hand sides of Eq. (46), $X_{n_{P;j}}$ values at intersections are solutions for distinct pairs of $(\rho_{n_{P;j}}, m_j)$.

which, by introducing normalization constants $A_{n_{P;j},\max/\min}$, limits the decay of the singular values

$$\sqrt{A_{n_{P;j},\min}\left(X_{n_{P;j},\min}\right)^\tau} \leq \Lambda^{n_{P;j}}_{j;\tau} \leq \sqrt{A_{n_{P;j},\max}\left(X_{n_{P;j},\max}\right)^\tau}, \tag{50}$$

and thus can be used to fix upper and lower bounds for the matrix dimensions required on the auxiliary bonds between physical and bath site. The normalization constants are determined from

$$\rho_{n_{P;j}} = A_{n_{P;j},\eta}\sum_{\tau=1}^{m_j}\left(X_{n_{P;j},\eta}\right)^\tau = A_{n_{P;j},\eta}X_{d,\eta}\frac{1-\left(X_{n_{P;j},\eta}\right)^{m_j}}{1-X_{n_{P;j},\eta}}$$

$$\Rightarrow A_{n_{P;j},\eta} = \frac{1-X_{n_{P;j},\eta}}{X_{n_{P;j},\eta}}\frac{\rho_{n_{P;j}}}{1-\left[X_{n_{P;j},\eta}\right]^{m_j}}, \tag{51}$$

with $\eta = \min, \max$. We introduce a truncation threshold $\delta'_{n_{P;j}}$ for each block so that for singular values with $\tau \leq m'_{n_{P;j},\eta} \leq m_j$, we obtain

$$\rho_{n_{P;j}} - \delta'_{n_{P;j}} \geq A_{n_{P;j},\eta}\sum_{\tau=1}^{m'_{n_{P;j},\eta}}\left(X_{n_{P;j},\eta}\right)^\tau = \rho_{n_{P;j}}\frac{1-\left[X_{n_{P;j},\eta}\right]^{m'_{n_{P;j},\eta}}}{1-\left(X_{n_{P;j},\eta}\right)^{m_j}}$$

$$\Rightarrow \left[X_{n_{P;j},\eta}\right]^{m'_{n_{P;j},\eta}} \geq 1 - \left(1 - \frac{\delta'_{n_{P;j}}}{\rho_{n_{P;j}}}\right)\left(1-\left(X_{n_{P;j},\eta}\right)^{m_j}\right). \tag{52}$$

For this inequality to hold, we necessarily need $\rho_{n_{P;j}} - \delta'_{n_{P;j}} \geq 0$, because $A_{n_{P;j},\eta}, X_{n_{P;j},\eta} > 0$. This is ensured by taking $n_{P;j} \in \mathcal{D}$ and choosing $\delta'_{n_{P;j}} = \max(\frac{\delta}{|\mathcal{D}|}, \min_{n_{P;j}\in\mathcal{D}}\rho_{n_{P;j}})$ as
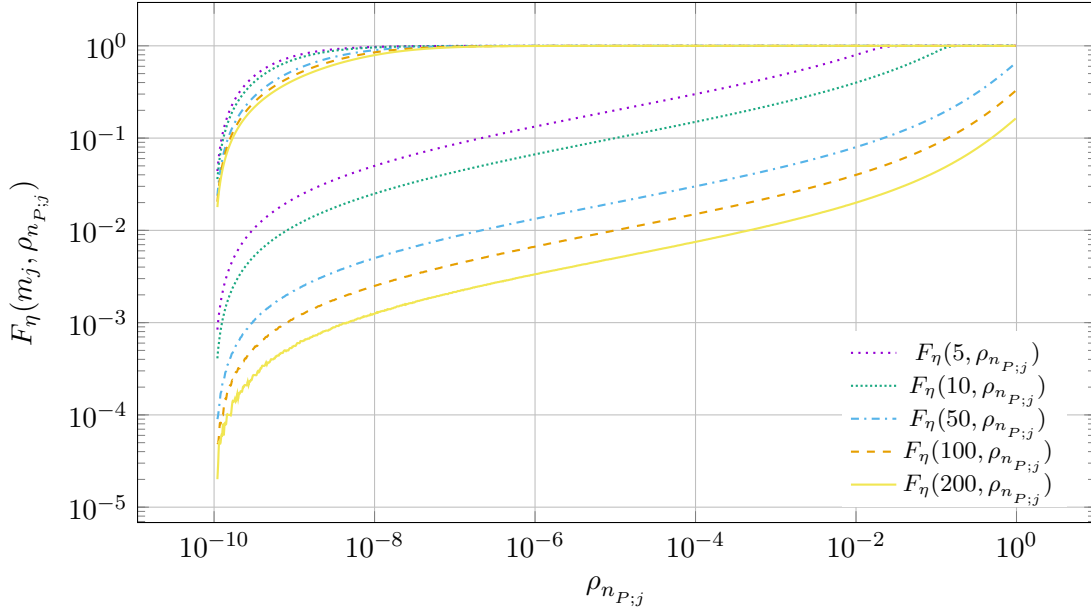
Figure 9: Upper and lower bounds $F_{\max/\min}(m_j, \rho_{n_{P;j}})$ for relative change in bond dimension $\dfrac{m'_{n_{P;j}}}{m_j}$ per tensor block on bond between physical and auxiliary sites derived from Eq. (46).

truncation scheme. Then, taking the logarithm of both sides and solving for $m'_{n_{P;j},\eta}$, we divide by $\log X_{n_{P;j},\eta} < 0$ so that

$$ m'_{n_{P;j},\eta} \leq \frac{\log \left\{ 1 - \left(1 - R_{n_{P;j}}\right)\left(1 - \left[X_{n_{P;j},\eta}\right]^{m_j}\right)\right\}}{\log X_{n_{P;j},\eta}} \,, \tag{53}$$

where we defined the truncation ratio $R_{n_{P;j}} = \dfrac{\delta'_{n_{P;j}}}{\rho_{n_{P;j}}} \leq 1$. Imposing equality between the left and right side, we finally obtain an estimation for the upper and lower bounds of the required bond dimension $m'_{n_{P;j},\eta}$ in each block. Introducing the relative change of the number of kept states $F_\eta(m_j, \rho_{n_{P;j}}) = \dfrac{m'_{n_{P;j},\eta}}{m_j}$, we show the bounds in Fig. 9 for varying m_j and $\rho_{n_{P;j}}$. For the upper bound there are two regimes: In the limit of small truncation ratio $R_{n_{P;j}} \ll 1$ we have $F_{n_{P;j},\max}(m_j, \rho_{n_{P;j}}) \approx 1$, whereas for $R_{n_{P;j}} \to 1$ there is a sharp drop towards zero. The transition regime between both asymptotics is governed by the physical bond dimension m_j and shifts towards larger values of $\rho_{n_{P;j}}$ as m_j increases. The lower bound exhibits a power-law decay over several magnitudes of $\rho_{n_{P;j}}$ and saturates towards one if m_j is small (Fig. 9). Finally, from Fig. 8 we can deduce that if $m_j \gg 1$, the lower bound becomes an increasingly better approximation for the bond dimension $m'_{n_{P;j},j}$.

In summary, we found that for small physical bond dimension m_j characterizing the approximation of the state without bath sites, the bond dimension $m'_{j,n_{P;j}}$ between physical and auxiliary sites is of the order of $|\mathcal{D}'|m_j$ if m_j is small ($\sim \mathcal{O}(1)$) and $\mathcal{D}' = \left\{ n_{P;j} \mid \rho_{n_{P;j}} > \delta \right\}$. However, if $m_j \gg 1$, the relative value of the bond dimension m'_{j,n_P^P} per tensor block compared to m_j mostly follows a power law in $\rho_{n_{P;j}}$ and quickly decays

to zero. In this situation, the state can be efficiently approximated in the enlarged Hilbert space with a moderate growth of the bond dimension, given that the occupations of the single-site reduced density matrix $\rho_{n_{P;j}}$ decay fast enough.

In physical problems one is often faced with exponentially decaying occupations of $\rho_{n_{P;j}}$ [48, 49]. Exemplary, we consider a typical, physical bond dimension $m_j = 100$ and assume $\rho_{n_{P;j}} \propto e^{-2n_{P;j}}$ with a truncation threshold of $\delta = 10^{-14}$ and take into consideration a local dimension of $n_{P;j} = 21$ (i.e., permit for 20 occupied states). We use the derived lower bound and obtain $m'_j \approx m_j$. This estimation relies on the assumption of strictly exponentially decaying singular values in each tensor block, which does not necessarily need to be the case in actual calculations. However, a relative growth in the overall bond dimension of $\mathcal{O}(1)$ was also found in our test calculations. Finally, we note that due to the rapid decrease of the lower bound derived above the total local dimension $n_{P;j}$ is not a limiting factor in the first place as long as m_j is large enough. In turn, the decay of the reduced single-site density matrix occupation strongly dictates the numerical expenses.

We close this section by demonstrating the numerical benefits of the above introduced enlargement of the Hilbert space and projection into the subspace $\mathcal{P}$ by considering the scaling of the most expensive calculation in a DMRG two-site ground-state search. This algorithm scales with the application of the MPO to the MPS and has dominating numerical expenses $m_j^3 \cdot w_j \cdot n_{P;j}^2$ if m_j is sufficiently larger than w_j. Assuming a typical growth factor 2 between the physical and bath sites, this operation is 8 times more expensive on these bonds than on the original bond between physical sites only. In order to benefit from the introduction of $U(1)$-invariant state representations in the first place, we therefore need to have a reasonably large local dimension $n_{P;j} > \sqrt{8}$, since for $U(1)$-invariant representations all local generators can be chosen as one-dimensional representations. Thus, $n_{P;j} \geq 3$ already speeds up this contraction and the benefits will grow quadratically with larger $n_{P;j}$. We may also consider a decomposition of the MPO bond dimension w_j due to the $U(1)$ symmetry, which typically is of the order of $2 - 3$ and thereby also generates an additional speed-up. Finally, we note that the system size is doubled, which could also be incorporated into the estimations. But this is only a constant factor of two and can be compensated easily by the quadratically growing expenses in the local dimension or the decomposition of the MPO bond dimension under the global symmetry.

6 Examples

In this section, we provide two simple examples, namely the Holstein model and the Hubbard model with superconducting (SC) terms. We concentrate on some technical details for the latter system, and present and discuss numerical results of the former.

6.1 Holstein Model

The Holstein model [50] is given by

$$\hat{H} = -t \sum_j \left(\hat{c}_j^\dagger \hat{c}_{j+1} + \text{h.c.} \right) + \omega_0 \sum_j \hat{b}_j^\dagger \hat{b}_j + \gamma \sum_j \hat{n}_j^f \left(\hat{b}_j^\dagger + \hat{b}_j \right) , \qquad (54)$$

in which $\hat{c}_j^{(\dagger)}$ denotes spinless fermion annihilation (creation) operators, $\hat{n}_j^f = \hat{c}_j^\dagger \hat{c}_j$ the corresponding particle number operators, and $\hat{b}_j^{(\dagger)}$ the bosonic annihilation (creation) operators. The parameters of this model are the hopping amplitude t, the phonon frequency

ω_0, and the electron-phonon coupling γ. Here, the total number of spinless fermions $\sum_j \hat{n}_j^f$ is conserved, while the total number of phonons $\sum_j \hat{b}_j^\dagger \hat{b}_j$ is not. Owing to the fermion-phonon interaction, the number of phonons per lattice site can become very large, rendering this model very challenging for DMRG, in particular in the charge-density wave (CDW) phase at half filling [6,7], for which we also present some numerical results.

We restore the conservation of the global phonon number by adding balancing operators $\hat{\beta}_{B;j}^{(\dagger)}$, according to the procedure described in Sec. 3. The projected purified Hamilton operator then reads

$$\hat{H}_{PP} = -t \sum_j \left(\hat{c}_{P;j}^\dagger \hat{c}_{P;j+1} + \text{h.c.} \right) + \omega_0 \sum_j \hat{b}_{P;j}^\dagger \hat{b}_{P;j} + \gamma \sum_j \hat{n}_j^f \left(\hat{b}_{P;j}^\dagger \hat{\beta}_{B;j} + \hat{b}_{P;j} \hat{\beta}_{B;j}^\dagger \right) . \tag{55}$$

Note that the local phonon-density operators transform as $\hat{b}_j^\dagger \hat{b}_j \to \hat{b}_{P;j}^\dagger \hat{b}_{P;j}$ since $\hat{\beta}_{B;j}^\dagger \hat{\beta}_{B;j} = 1$. Here, the last identity follows from the specific definition of the balancing operators in Eqs. (17) and (18).

Numerical results in the CDW phase
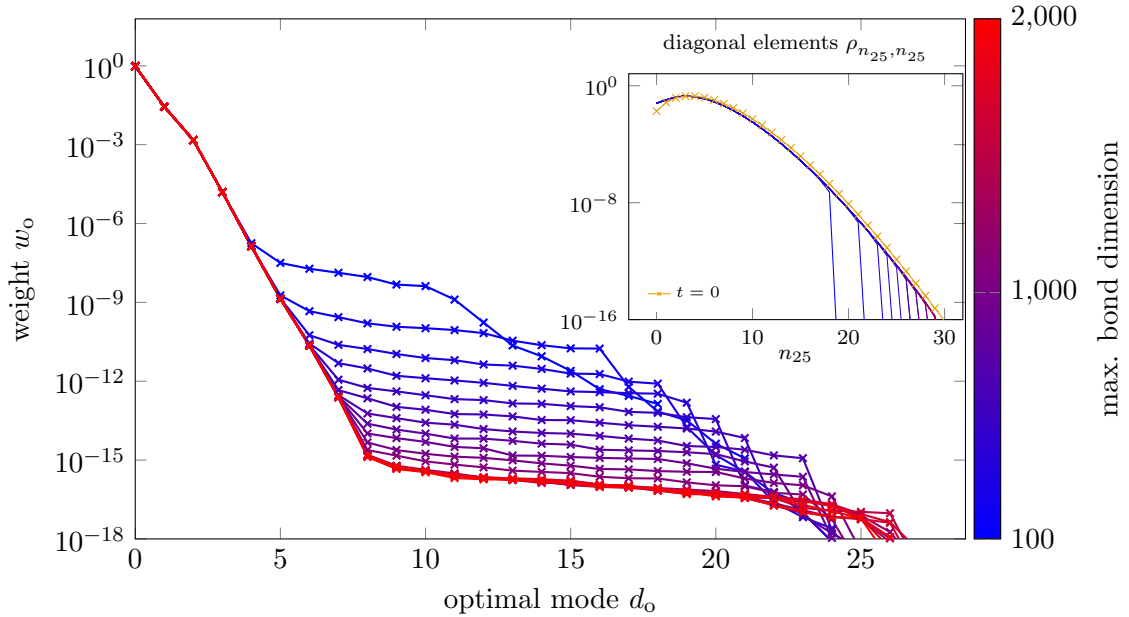
Figure 10: Weight w_{o} of optimal modes d_{o} as a function of the maximal bond dimension at the auxiliary bond γ_{25} using the projected purification. Data is extracted from the single-site reduced density matrix $\rho_{n_{25},n'_{25}}$ at the center site ($j = 25$) in the calculated ground state of the half-filled Holstein model with $L = 51$ sites and $N = 25$ fermions, $\omega/t = 1.0, \gamma/t = 2.0$. The inset shows the diagonal elements $\rho_{n_{25},n_{25}}$ indicating the immediate effect of truncations. For comparison the phonon-excitation probabilities obtained for $t = 0$ are overlayed, indicated by yellow crosses.

In order to illustrate the numerical properties of the mapping introduced in this paper, we performed calculations in the CDW phase of the half-filled Holstein model [7,40,51]. This phase is characterized by the formation of bound electron-phonon states (polarons) and a Fermi wave vector $k_F = \pi$, i.e., in a physical image every second lattice site is occupied by a polaron. In the atomic limit $t \to 0$, there is an analytic expression for the

probability $P_{\text{ph}}(n_j)$ to measure n_j phonons at occupied lattice sites j, which is given by

$$P_{\text{ph}}(n_j) = \frac{\gamma^{2n_j}}{\omega_0^{2n_j} n_j!} e^{-\frac{\gamma^2}{\omega_0^2}} \ . \tag{56}$$

Note that the excitation probabilities are given by the diagonal elements of the single-site reduced density matrix. Hence, they can be evaluated directly numerically. Another important quantity is the occupation w_0 of the optimal modes of the single-site reduced density matrix $\hat{\rho}_j$, which was already mentioned in Sec. 5.1. The optimal modes $|d_{\text{o}}\rangle$ are the eigenstates of $\hat{\rho}_j$ and their occupations are the corresponding eigenvalues

$$\hat{\rho}_j = \sum_{d_{\text{o}}} w_{\text{o}} |d_{\text{o}}\rangle \langle d_{\text{o}}| \ . \tag{57}$$

As discussed elsewhere [13, 40, 42], these constitute an important measure for the quality of the approximation of the phonon states. In our framework, the full reduced single-site density matrix can be extracted directly from the projected purified state $|\psi)$ in a mixed canonical representation when contracting physical and bath site tensors $T^{n_{P/B;j}}$ over their auxiliary bond index γ_{j-1} (see Eq. (29)):

$$\hat{\rho}_{j;n_j,n_j'} = \text{Tr}_{k \neq j} |\psi) (\psi| = \text{Tr}\left\{ \left[T^{n_{P;j}'} T^{n_{B;j}'} \right]^\dagger T^{n_{P;j}} T^{n_{B;j}} \right\} \ , \tag{58}$$

where we used the mapping I to identify $n_{P;j} \equiv n_j$ (see also Eq. (38)).

For our calculations, we set $\omega_0/t = 1.0$ and $\gamma/t = 2.0$ so that the model is in the CDW phase. In Fig. 10, the optimal modes of a system with $L = 51$ sites and $N = 25$ fermions are displayed for the ground-state and on an occupied lattice site ($j = 25$). The truncation was performed by allowing a maximum discarded weight of $\delta = 10^{-14}$ per auxiliary bond while restricting the total bond dimension to $m_j \leq 2000$. The color-coded graphs correspond to calculations with different, maximally allowed total bond dimensions.

The immediate effect of the truncation on the auxiliary bonds between physical and bath site tensors can be seen as a suppression of the occupation w_{o} of optimal modes when w_{o} becomes small. Upon increasing the total bond dimension m_j, the distribution $w_{\text{o}}(d_{\text{o}})$ becomes stationary once $m_j > 1200$. In the inset, the diagonal elements of the single-site reduced density matrix are shown as a function of m_j and overlayed with the occupation probabilities $P_{\text{ph}}(n_j)$ (Eq. (56)) in the atomic limit. The discarded diagonal elements of $\hat{\rho}_j$ can be deduced from the intersection of the vertical lines with the horizontal axis. Comparing the magnitude at which diagonal elements of $\hat{\rho}_j$ are discarded as a function of m_j to the plateaus of the optimal mode occupation in the main plot, we find a clear correspondence between both. This can be related to the discussion in Sec. 5.1, where we showed that w.r.t. to the 1-norm the quality of the approximation of the projected purified state is bounded by the occupation of the optimal modes of $\hat{\rho}_j$, which are not treated correctly. Thus, a scaling analysis in the bond dimension m_j only is sufficient to obtain converged results for the phonon system. Finally, we find that, in accordance with the system being deep in the CDW phase, the diagonal elements $\rho_{j;n_j,n_j}$ are already very close to the excitation probabilities $P_{\text{ph}}(n_j)$ in the atomic limit. Even though the bond dimensions $m_j \leq 2000$ may appear very large, the fact that we are able to exploit global $U(1)$ symmetries for both the fermionic and bosonic system allows us to perform these calculations very efficiently.

We also performed a finite-size scaling of the ground-state energy E_δ as a function of the discarded weight per bond to prove the capability of our approach to deal with large system sizes. Here, we applied a scaling analysis in the numerical precision, tuning the
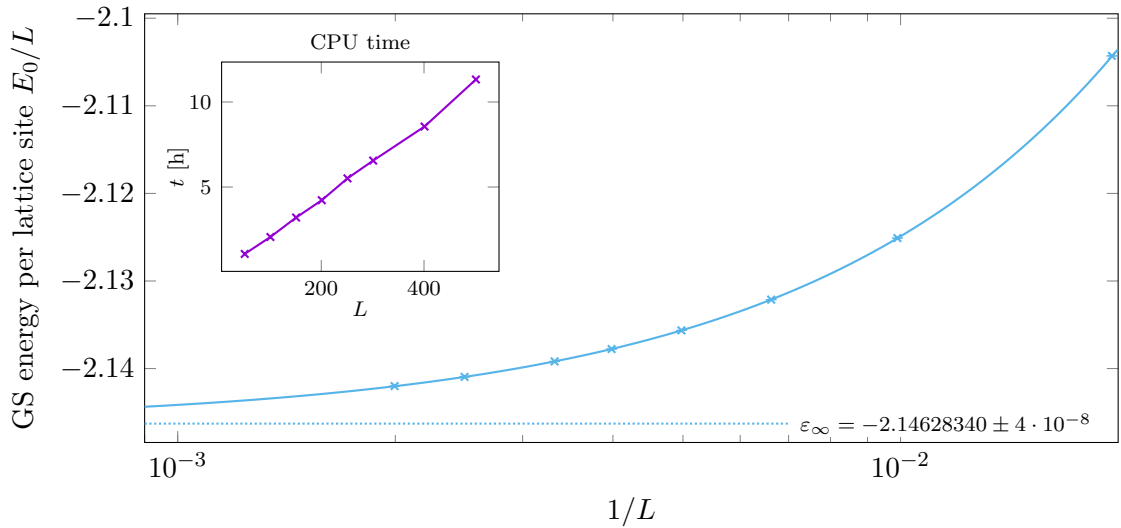
Figure 11: Finite-size scaling for the ground-state energy of the Holstein model at half filling using the projected purification and a two-site DMRG solver. The model is evaluated for parameters $\omega/t = 1.0$, $\gamma/t = 2.0$ at nearly half filling and a maximum discarded weight per bond $\delta = 10^{-10}$. We chose system sizes $L = 51, 101, 151, 201, 251, 301, 401, 501$ and electron fillings $N_{\mathrm{el}} = (L-1)/2$. The inset shows the total CPU time for the ground-state search as a function of the number of lattice sites L.

maximal discarded weight per bond from $\delta = 10^{-4}$ to $\delta = 10^{-10}$ and extrapolated E_0 towards $\delta \to 0$. The number of lattice sites was increased from $L = 51$ sites up to $L = 501$ sites. In Fig. 11, we show the extrapolations and the scaling of the intensive energy density E_0/L as a function of $1/L$. We fit the ground-state energy densities as a function of the number of lattice sites using the ansatz

$$\frac{E_0}{L} = \frac{A}{L} + \varepsilon_\infty \ . \tag{59}$$

Here, $\lim_{L \to \infty} E_0/L = \varepsilon_\infty$ is the extrapolated ground-state energy density in the thermodynamic limit yielding

$$\varepsilon_\infty = -2.14628340 \pm 4 \cdot 10^{-8} \ . \tag{60}$$

Note that the given uncertainty is obtained from propagating the errors of the scaling w.r.t. to the discarded weight per bond, which was done for each lattice size L. Since bond observables are evaluated with errors whose absolute values are bounded by the discarded weight per bond, this is a numerically exact error bound. Additionally, in the inset of Fig. 11, we plot the total CPU time of a ground-state search running until the convergence threshold $L\delta$ with $\delta = 10^{-8}$ for the relative change in the ground-state energy after a completed sweep was reached. Using two cores of an Intel® Xeon® Gold 6150 CPU @ 2.70GHz, the largest systems with $L = 501$ converged after ~ 12 hours.

6.2 Hubbard Model with pair creation and annihilation

The Hubbard model [52–57] with additional SC terms is given by

$$\hat{H} = -t \sum_{j,\sigma} \left(\hat{c}^\dagger_{j,\sigma} \hat{c}_{j+1,\sigma} + \text{h.c.} \right) + U \sum_j \hat{n}_{j,\uparrow} \hat{n}_{j,\downarrow} + \Delta \sum_j \left(\hat{c}^\dagger_{j,\uparrow} \hat{c}^\dagger_{j,\downarrow} + \text{h.c.} \right) \ , \tag{61}$$

in which $\hat{c}_j^{(\dagger)}$ denotes spin $S = 1/2$ fermion annihilation (creation) operators and $\hat{n}_j = \sum_{\sigma=\uparrow,\downarrow} \hat{c}_{j,\sigma}^\dagger \hat{c}_{j,\sigma}$ the local fermion density operator. The parameters of this model are the hopping amplitude t, the interaction strength U, and the SC pair creation and annihilation amplitude Δ.

In this model, the pair creation contributions $\propto \Delta$ break the conservation of the global particle number conservation. We restore the corresponding global $U(1)$ symmetry by adding balancing operators $\hat{\beta}_{B;j,\sigma}^{(\dagger)}$ with $\sigma = \uparrow, \downarrow$. The projected purified Hamiltonian now reads

$$
\begin{aligned}
\hat{H}_{PP} = & - t \sum_{j,\sigma} \left(\hat{c}_{P;j,\sigma}^\dagger \hat{\beta}_{B;j,\sigma} \hat{c}_{P;j+1,\sigma} \hat{\beta}_{B;j+1,\sigma}^\dagger + \text{h.c.} \right) + U \sum_j \hat{n}_{B;j,\uparrow} \hat{n}_{B;j,\downarrow} \\
& + \Delta \sum_j \left(\hat{c}_{j,\uparrow}^\dagger \hat{\beta}_{B;j,\uparrow} \hat{c}_{j,\downarrow}^\dagger \hat{\beta}_{B;j,\downarrow} + \text{h.c.} \right) .
\end{aligned}
\tag{62}
$$

Again, the local density terms remain unchanged due to $\hat{\beta}_{B;j,\sigma}^\dagger \hat{\beta}_{B;j,\sigma} = 1$. Exploiting this representation, one of the authors studied the charge-degeneracy points of topologically superconducting islands coupled to normal leads [58–61].

In contrast to the Holstein model, here the projected purification acts on fermions. This causes a subtilty if the fermionic anticommutation relations are implemented in terms of Jordan-Wigner strings [62] as is usually done, either explicitly or implicitly. For instance, if $\hat{b}_{j,\uparrow}^{(\dagger)}$ are annihilation (creation) operators of hardcore bosons at lattice j, then fermionic, bilinear operators can be written in terms of parity operators $\hat{P}_{\hat{b}_{j,\uparrow}}$ as

$$
\hat{c}_{j,\uparrow}^\dagger \hat{c}_{j+k,\uparrow} = \hat{b}_j^\dagger \left[\prod_{l=1}^{k} \hat{P}_{\hat{b}_{j+l,\uparrow}} \right] \hat{b}_{j+k,\uparrow}.
\tag{63}
$$

The operator string $\prod_{l=1}^{k} \hat{P}_{\hat{b}_{j+l,\uparrow}}$ is commonly referred to as Jordan-Wigner string and a consequence of the anticommutation relations. The problem here is that mapping such operator strings into the purified Hilbert space, one has to ensure that they act only in the physical Hilbert space. For instance, if the generation of the anticommutation relations is implemented in the MPS code itself, then typically such Jordan-Wigner strings are created automatically. If this is the case, their effect on the bath sites have to be canceled, which can be done by placing parity operators on bath sites inside the Jordan-Wigner string, for instance,

$$
\hat{c}_{j,\uparrow}^\dagger \hat{c}_{j+k,\uparrow} \rightarrow \hat{c}_{j,\uparrow}^\dagger \hat{\beta}_{B;j} \left[\prod_{l=0}^{k-1} \hat{P}_{\hat{b}_{B;j+l,\uparrow}} \right] \hat{c}_{j+k,\uparrow} \hat{\beta}_{B;j}^\dagger .
\tag{64}
$$

7 Conclusion

Numerically studying strongly correlated quantum many-body systems with a large number of local degrees of freedom is a challenging problem, in particular for tensor-network methods [6, 7, 40–42]. In this paper we address the problem by introducing a mapping (projected purification) to construct artificial, global $U(1)$ symmetries for models without a generic $U(1)$ symmetry. For any given operator acting on a tensor-product Hilbert space $\mathcal{H}$, we derived a construction scheme that generates its projected purified representation in a subspace of the thermofield doubling of $\mathcal{H}$. We show that both operators can be

identified with each other by an isomorphism, but the projected purified representation manifestly conserves global $U(1)$ symmetries. Additionally, we derive a projected purified representation of MPS exploiting the fact that the isomorphism is obtained from a gauge fixing of the additional degrees of freedom introduced by the doubling. Here, the tensors representing the projected purified state can exploit the restored global $U(1)$ symmetry which, for instance, immediately reduces the effective local dimension in each tensor block to 1 providing a significant speedup during numerical calculations when the local Hilbert space dimension is large. We characterize this representation and reveal an intimate relation between the Schmidt values of projected purified MPS and the single-site reduced density matrix that allows us to estimate the numerical expenses of our representation in comparison to calculations without symmetries.

The mapping into a projected purified representation of operators and states is mostly independent of the underlying implementation. Thereby, it can be used without much effort with already existing toolkits, which we demonstrated by performing numerical calculations [63] on the one-dimensional Holstein model at half filling [7, 10, 51, 64]. The large number of local degrees of freedom that have to be taken into account (we allow up to $N_{\mathrm{ph}} = 63$ phonons per lattice site) renders large scale calculations very challenging. We perform a finite-size scaling in the CDW phase taking into account a maximum number of $L = 501$ lattice sites while maintaining a high numerical precision and keeping up to $m_{\max} = 2000$ states per bond.

Due to the reduction of the effective local dimension of the MPS blocks, two-site solvers with a larger numerical complexity can be used [30,31,37,65], as we did in the ground-state calculations of the Holstein model. Therefore, the projected purification allows to apply two-site time-dependent variational principle (2TDVP) [32,66] as time evolution method to treat systems out of equilibrium. So far, existing methods to tackle such problems mostly [67] use time-evolving block decimation (TEBD) as time stepper, only, due to the high numerical costs when performing two-site updates on systems with a large number of local degrees of freedom [13]. However, TEBD typically requires a much smaller time step to achieve a certain precision, compared to 2TDVP [33]. We thus anticipate that using the presented mapping, out of equilibrium and finite-temperature calculations of such highly complicated systems can become cheaper, more reliable, and straight forward to realize. For instance, we expect this mapping to enable the efficient application of tensor-network algorithms to address questions about lattice electrons coupled to phonons out of equilibrium [22,68,69], numerically unbiased. Furthermore, our mapping is compatible with common MPO-based time-evolution methods, e.g., the aforementioned TEBD as well as the MPO $W^{\mathrm{I,II}}$ methods [70]. Exhibiting a scaling of the numerical complexity that is at least quadratic in the local dimension [33], these time-evolution schemes should also benefit from taking operators to their projected purified representation.

Acknowledgements   We thank A. Feiguin, K. Harms, F. Heidrich-Meisner, A. Kantian, R. K. Kessing, and S. R. Manmana for insightful discussions. TK acknowledges financial support by the ERC Starting Grant from the European Union's Horizon 2020 research and innovation program under grant agreement No. 758935. JS and SP were funded by the Deutsche Forschungsgemeinschaft (DFG, German Research Foundation) 207383564/FOR 1807 (projects P4 and P7). SP acknowledges support by the Deutsche Forschungsgemeinschaft (DFG, German Research Foundation) under Germany's Excellence Strategy-426 EXC-2111-390814868. We thank the TU Clausthal for providing access to the Nuku computational cluster.

A   Object comparison between LBO and ppDMRG

In this appendix, we aim to give an overview of the relationship between the objects used in the LBO and in the ppDMRG. Its main purpose is to support future discussions and developments. It is specifically not intended for implementation purposes, see Sec. 2.

In Fig. 12, a complete sandwich MPS-MPO-MPS for a single site is shown. In order to show the connection between the LBO and the ppDMRG, all tensors are split into virtual objects that are subsequently rejoined in different fashions. On the one hand, the objects coming from the LBO (highlighted with red boxes) are mainly split vertically into parts "belonging" to the physical and the bath Hilbert space. On the other hand, the objects coming from the ppDMRG (highlighted with blue boxes) needed to be split horizontally so that they could be related to the different objects in the LBO. In particular, the identities containing the maps I and $I^\dagger$ do not really appear within the ppDMRG.

Figure 12: A tensor network representing a single site consisting of an MPS, an MPO, and the adjoint MPS. All tensors are split into several (virtual) objects in order to be rejoined to the tensors used in the LBO (ppDMRG) as highlighted by the red (blue) boxes that contain virtual objects. Note that equivalent bond labels do not indicate the same objects, but only an implicit δ between the, for brevity not shown, different indicies.

References

[1] E. Berg, E. G. Dalla Torre, T. Giamarchi and E. Altman, Rise and fall of hidden string order of lattice bosons, Phys. Rev. B **77**, 245119 (2008), doi:10.1103/PhysRevB.77.245119.

[2] S. Ejima, M. J. Bhaseen, M. Hohenadler, F. H. L. Essler, H. Fehske and B. D. Simons, Ising deconfinement transition between feshbach-resonant superfluids, Phys. Rev. Lett. **106**, 015303 (2011), doi:10.1103/PhysRevLett.106.015303.

[3] I. Bloch, J. Dalibard and S. Nascimbene, Quantum simulations with ultracold quantum gases, Nat Phys **8**(4), 267 (2012).

[4] A. J. Daley, H. Pichler, J. Schachenmayer and P. Zoller, Measuring entanglement growth in quench dynamics of bosons in an optical lattice, Phys. Rev. Lett. **109**, 020505 (2012), doi:10.1103/PhysRevLett.109.020505.

[5] M. L. Wall, A. Safavi-Naini and A. M. Rey, Simulating generic spin-boson models with matrix product states, Phys. Rev. A **94**, 053637 (2016), doi:10.1103/PhysRevA.94.053637.

[6] E. Jeckelmann and S. R. White, Density-matrix renormalization-group study of the polaron problem in the Holstein model, Phys. Rev. B **57**, 6376 (1998), doi:10.1103/PhysRevB.57.6376.

[7] R. J. Bursill, R. H. McKenzie and C. J. Hamer, Phase diagram of the one-dimensional holstein model of spinless fermions, Phys. Rev. Lett. **80**, 5607 (1998), doi:10.1103/PhysRevLett.80.5607.

[8] R. J. Bursill, R. H. McKenzie and C. J. Hamer, Phase diagram of a heisenberg spin-peierls model with quantum phonons, Phys. Rev. Lett. **83**, 408 (1999), doi:10.1103/PhysRevLett.83.408.

[9] E. Jeckelmann, C. Zhang and S. R. White, Metal-insulator transition in the one-dimensional holstein model at half filling, Phys. Rev. B **60**, 7950 (1999), doi:10.1103/PhysRevB.60.7950.

[10] M. Tezuka, R. Arita and H. Aoki, Phase diagram for the one-dimensional Hubbard-Holstein model: A density-matrix renormalization group study, Phys. Rev. B **76**, 155114 (2007), doi:10.1103/PhysRevB.76.155114.

[11] B. Kloss, D. R. Reichman and R. Tempelaar, Multiset matrix product state calculations reveal mobile franck-condon excitations under strong holstein-type coupling, Phys. Rev. Lett. **123**, 126601 (2019), doi:10.1103/PhysRevLett.123.126601.

[12] D. Jansen, J. Stolpp, L. Vidmar and F. Heidrich-Meisner, Eigenstate thermalization and quantum chaos in the holstein polaron model, Phys. Rev. B **99**, 155130 (2019), doi:10.1103/PhysRevB.99.155130.

[13] J. Stolpp, J. Herbrych, F. Dorfner, E. Dagotto and F. Heidrich-Meisner, Charge-density-wave melting in the one-dimensional Holstein model, Physical Review B **101**(3) (2020), doi:10.1103/physrevb.101.035134.

[14] D. Jansen, J. Bonča and F. Heidrich-Meisner, Finite-temperature density-matrix renormalization group method for electron-phonon systems: Thermodynamics and holstein-polaron spectral functions (2020), `2007.11343`.

[15] A. Nocera, J. Sous, A. E. Feiguin and M. Berciu, One-dimensional peierls phase separation in the dilute carrier density limit (2020), 2008.03304.

[16] F. F. Assaad and T. C. Lang, Diagrammatic determinantal quantum monte carlo methods: Projective schemes and applications to the hubbard-holstein model, Phys. Rev. B **76**, 035116 (2007), doi:10.1103/PhysRevB.76.035116.

[17] M. Hohenadler and G. G. Batrouni, Dominant charge density wave correlations in the holstein model on the half-filled square lattice, Physical Review B **100**(16) (2019), doi:10.1103/physrevb.100.165114.

[18] E. V. Boström, P. Helmer, P. Werner and C. Verdozzi, Electron-electron versus electron-phonon interactions in lattice models: Screening effects described by a density functional theory approach, Physical Review Research **1**(1) (2019), doi:10.1103/physrevresearch.1.013017.

[19] T. E. Reinhard, U. Mordovina, C. Hubig, J. S. Kretchmer, U. Schollwöck, H. Appel, M. A. Sentef and A. Rubio, Density-matrix embedding theory study of the one-dimensional hubbard–holstein model, Journal of Chemical Theory and Computation **15**(4), 2221–2232 (2019), doi:10.1021/acs.jctc.8b01116.

[20] P. Werner and A. J. Millis, Efficient dynamical mean field simulation of the holstein-hubbard model, Phys. Rev. Lett. **99**, 146404 (2007), doi:10.1103/PhysRevLett.99.146404.

[21] M. Schüler, M. Eckstein and P. Werner, Truncating the memory time in nonequilibrium dynamical mean field theory calculations, Physical Review B **97**(24) (2018), doi:10.1103/physrevb.97.245129.

[22] S. Sayyad, R. Žitko, H. U. R. Strand, P. Werner and D. Golež, Comparative study of nonequilibrium insulator-to-metal transitions in electron-phonon systems, Physical Review B **99**(4) (2019), doi:10.1103/physrevb.99.045118.

[23] S. R. White, Density matrix formulation for quantum renormalization groups, Phys. Rev. Lett. **69**(19), 2863 (1992), doi:10.1103/PhysRevLett.69.2863.

[24] S. R. White, Density-matrix algorithms for quantum renormalization groups, Phys. Rev. B **48**(14), 10345 (1993), doi:10.1103/PhysRevB.48.10345.

[25] S. Rommer and S. Östlund, Class of ansatz wave functions for one-dimensional spin systems and their relation to the density matrix renormalization group, Phys. Rev. B **55**, 2164 (1997), doi:10.1103/PhysRevB.55.2164.

[26] G. Vidal, Efficient simulation of one-dimensional quantum many-body systems, Phys. Rev. Lett. **93**, 040502 (2004), doi:10.1103/PhysRevLett.93.040502.

[27] A. J. Daley, C. Kollath, U. Schollwöck and G. Vidal, Time-dependent density-matrix renormalization-group using adaptive effective Hilbert spaces, Journal of Statistical Mechanics: Theory and Experiment **2004**(04), P04005 (2004).

[28] S. R. White and A. E. Feiguin, Real-time evolution using the density matrix renormalization group, Phys. Rev. Lett. **93**, 076401 (2004), doi:10.1103/PhysRevLett.93.076401.

[29] F. Verstraete and J. I. Cirac, Matrix product states represent ground states faithfully, Phys. Rev. B **73**, 094423 (2006), doi:10.1103/PhysRevB.73.094423.

[30] U. Schollwöck, The density-matrix renormalization group, Rev. Mod. Phys. **77**, 259 (2005), doi:10.1103/RevModPhys.77.259.

[31] U. Schollwöck, The density-matrix renormalization group in the age of matrix product states, Annals of Physics **326**(1), 96 (2011), doi:DOI: 10.1016/j.aop.2010.09.012, January 2011 Special Issue.

[32] J. Haegeman, C. Lubich, I. Oseledets, B. Vandereycken and F. Verstraete, Unifying time evolution and optimization with matrix product states, Phys. Rev. B **94**, 165116 (2016), doi:10.1103/PhysRevB.94.165116.

[33] S. Paeckel, T. Köhler, A. Swoboda, S. R. Manmana, U. Schollwöck and C. Hubig, Time-evolution methods for matrix-product states, Annals of Physics **411**, 167998 (2019), doi:10.1016/j.aop.2019.167998.

[34] I. P. McCulloch, From density-matrix renormalization group to matrix product states, Journal of Statistical Mechanics: Theory and Experiment **2007**(10), P10014 (2007).

[35] S. Singh, R. N. C. Pfeifer and G. Vidal, Tensor network decompositions in the presence of a global symmetry, Phys. Rev. A **82**, 050301 (2010), doi:10.1103/PhysRevA.82.050301.

[36] S. Singh, R. N. C. Pfeifer and G. Vidal, Tensor network states and algorithms in the presence of a global U(1) symmetry, Phys. Rev. B **83**, 115125 (2011), doi:10.1103/PhysRevB.83.115125.

[37] C. Hubig, Abelian and non-abelian symmetries in infinite projected entangled pair states, SciPost Physics **5**(5) (2018), doi:10.21468/scipostphys.5.5.047.

[38] M. Fannes, B. Nachtergaele and R. Werner, Finitely correlated states on quantum spin chains, Communications in Mathematical Physics **144**, 443 (1992).

[39] J. Eisert, M. Cramer and M. B. Plenio, Colloquium: Area laws for the entanglement entropy, Rev. Mod. Phys. **82**(1), 277 (2010), doi:10.1103/RevModPhys.82.277.

[40] C. Zhang, E. Jeckelmann and S. R. White, Density matrix approach to local Hilbert space reduction, Phys. Rev. Lett. **80**, 2661 (1998), doi:10.1103/PhysRevLett.80.2661.

[41] C. Guo, A. Weichselbaum, J. von Delft and M. Vojta, Critical and strong-coupling phases in one- and two-bath spin-boson models, Phys. Rev. Lett. **108**, 160401 (2012), doi:10.1103/PhysRevLett.108.160401.

[42] C. Brockt, F. Dorfner, L. Vidmar, F. Heidrich-Meisner and E. Jeckelmann, Matrix-product-state method with a dynamical local basis optimization for bosonic systems out of equilibrium, Phys. Rev. B **92**, 241106 (2015), doi:10.1103/PhysRevB.92.241106.

[43] A. E. Feiguin and S. R. White, Finite-temperature density matrix renormalization using an enlarged hilbert space, Phys. Rev. B **72**, 220401 (2005), doi:10.1103/PhysRevB.72.220401.

[44] F. Verstraete, J. J. García-Ripoll and J. I. Cirac, Matrix product density operators: Simulation of finite-temperature and dissipative systems, Phys. Rev. Lett. **93**, 207204 (2004), doi:10.1103/PhysRevLett.93.207204.

[45] T. Barthel, U. Schollwöck and S. R. White, Spectral functions in one-dimensional quantum systems at finite temperature using the density matrix renormalization group, Phys. Rev. B **79**(24), 245101 (2009), doi:10.1103/PhysRevB.79.245101.

[46] P. Fayet and S. Ferrara, Supersymmetry, Physics Reports **32**(5), 249 (1977), doi:https://doi.org/10.1016/0370-1573(77)90066-7.

[47] R. Penrose, Applications of negative dimensional tensors, Combinatorial mathematics and its applications **1**, 221 (1971).

[48] F. Dorfner, L. Vidmar, C. Brockt, E. Jeckelmann and F. Heidrich-Meisner, Real-time decay of a highly excited charge carrier in the one-dimensional holstein model, Phys. Rev. B **91**, 104302 (2015), doi:10.1103/PhysRevB.91.104302.

[49] F. Dorfner and F. Heidrich-Meisner, Properties of the single-site reduced density matrix in the bose-bose resonance model in the ground state and in quantum quenches, Physical Review A **93**(6) (2016), doi:10.1103/physreva.93.063624.

[50] T. Holstein, Studies of polaron motion: Part i. the molecular-crystal model, Annals of Physics **8**(3), 325 (1959), doi:https://doi.org/10.1016/0003-4916(59)90002-8.

[51] C. E. Creffield, G. Sangiovanni and M. Capone, Phonon softening and dispersion in the 1D Holstein model of spinless fermions, The European Physical Journal B - Condensed Matter and Complex Systems **44**(2), 175 (2005), doi:10.1140/epjb/e2005-00112-9.

[52] M. C. Gutzwiller, Effect of correlation on the ferromagnetism of transition metals, Phys. Rev. Lett. **10**, 159 (1963), doi:10.1103/PhysRevLett.10.159.

[53] J. Kanamori, Electron correlation and ferromagnetism of transition metals, Progress of Theoretical Physics **30**(3), 275 (1963), doi:10.1143/PTP.30.275, /oup/backfile/content_public/journal/ptp/30/3/10.1143/ptp.30.275/2/30-3-275.pdf.

[54] J. Hubbard, Electron correlations in narrow energy bands, Proceedings of the Royal Society of London A: Mathematical, Physical and Engineering Sciences **276**(1365), 238 (1963), doi:10.1098/rspa.1963.0204.

[55] J. Hubbard, Electron correlations in narrow energy bands. ii. the degenerate band case, Proceedings of the Royal Society of London A: Mathematical, Physical and Engineering Sciences **277**(1369), 237 (1964), doi:10.1098/rspa.1964.0019.

[56] J. Hubbard, Electron correlations in narrow energy bands. iii. an improved solution, Proceedings of the Royal Society of London A: Mathematical, Physical and Engineering Sciences **281**(1386), 401 (1964), doi:10.1098/rspa.1964.0190.

[57] J. Hubbard, Electron correlations in narrow energy bands. iv. the atomic representation, Proceedings of the Royal Society of London A: Mathematical, Physical and Engineering Sciences **285**(1403), 542 (1965), doi:10.1098/rspa.1965.0124.

[58] R. M. Lutchyn, J. D. Sau and S. Das Sarma, Majorana fermions and a topological phase transition in semiconductor-superconductor heterostructures, Phys. Rev. Lett. **105**, 077001 (2010), doi:10.1103/PhysRevLett.105.077001.

[59] R. M. Lutchyn, E. P. A. M. Bakkers, L. P. Kouwenhoven, P. Krogstrup, C. M. Marcus and Y. Oreg, Majorana zero modes in superconductor–semiconductor heterostructures, Nature Reviews Materials **3**(5), 52–68 (2018), doi:10.1038/s41578-018-0003-1.

[60] A. Keselman, C. Murthy, B. van Heck and B. Bauer, Spectral response of josephson junctions with low-energy quasiparticles, SciPost Physics **7**(4) (2019), doi:10.21468/scipostphys.7.4.050.

[61] S. Paeckel, Topological and non-equilibrium superconductivity in low-dimensional strongly correlated quantum systems, Ph.D. thesis, Universität Göttingen (2020).

[62] S. Paeckel, T. Köhler and S. R. Manmana, Automated construction of $U(1)$-invariant matrix-product operators from graph representations, SciPost Phys. **3**, 035 (2017), doi:10.21468/SciPostPhys.3.5.035.

[63] S. Paeckel and T. Köhler, Symmps, `https://www.symmps.eu`, Accessed: 2019-12-29.

[64] J. E. Hirsch and E. Fradkin, Phase diagram of one-dimensional electron-phonon systems. ii. the molecular-crystal model, Phys. Rev. B **27**, 4302 (1983), doi:10.1103/PhysRevB.27.4302.

[65] C. Hubig, J. Haegeman and U. Schollwöck, Error estimates for extrapolations with matrix-product states, Physical Review B **97**(4) (2018), doi:10.1103/physrevb.97.045125.

[66] J. Haegeman, J. I. Cirac, T. J. Osborne, I. Pižorn, H. Verschelde and F. Verstraete, Time-dependent variational principle for quantum lattices, Phys. Rev. Lett. **107**, 070601 (2011), doi:10.1103/PhysRevLett.107.070601.

[67] F. A. Y. N. Schröder and A. W. Chin, Simulating open quantum dynamics with time-dependent variational matrix product states: Towards microscopic correlation of environment dynamics and reduced system evolution, Phys. Rev. B **93**, 075105 (2016), doi:10.1103/PhysRevB.93.075105.

[68] P. Werner and M. Eckstein, Phonon-enhanced relaxation and excitation in the holstein-hubbard model, Physical Review B **88**(16) (2013), doi:10.1103/physrevb.88.165108.

[69] M. Weber, F. F. Assaad and M. Hohenadler, Phonon spectral function of the one-dimensional holstein-hubbard model, Physical Review B **91**(23) (2015), doi:10.1103/physrevb.91.235150.

[70] M. P. Zaletel, R. S. K. Mong, C. Karrasch, J. E. Moore and F. Pollmann, Time-evolving a matrix product state with long-ranged interactions, Phys. Rev. B **91**, 165112 (2015), doi:10.1103/PhysRevB.91.165112.